OPEN ACCESS



Potassium Abundances in Extremely Metal Poor Stars: Implications for Nucleosynthesis in the Final Stages of Massive Star Evolution*

Miho N. Ishigaki^{1,2,3}, Nozomu Tominaga^{1,3,4}, Wako Aoki^{1,3}, Shinya Wanajo⁵, Tomoya Takiwaki^{1,3}, Ko Nakamura^{6,7}, Nobuyuki Iwamoto⁸, Ken'ichi Nomoto², and Chiaki Kobayashi^{2,9}, Shinya Wanajo⁵, National Astronomical Observatory of Japan 2-21-1, Mitaka, Tokyo 181-8588, Japan

National Astronomical Observatory of Japan 2-21-1, Mitaka, Tokyo 181-8588, Japan

Kavli Institute for the Physics and Mathematics of the Universe (WPI), The University of Tokyo Institutes for Advanced Study, The University of Tokyo, Kashiwa, Chiba 277-8583, Japan

Department of Astronomical Science, SOKENDAI (The Graduate University for Advanced Studies), 2-21-1 Osawa, Mitaka, Tokyo, 181-8588, Japan

Department of Physics, Konan University, 8-9-1 Okamoto, Kobe, Hyogo 658-8501, Japan

Astronomical Institute, Graduate School of Science, Tohoku University, 6-3 Aoba, Aramaki, Aoba-ku, Sendai, Miyagi 980-8578, Japan

Department of Applied Physics, Fukuoka University, Nanakuma Jonan 8-19-1, Fukuoka 814-0180, Japan

Research Institute of Stellar Explosive Phenomena, Fukuoka University, Nanakuma Jonan 8-19-1, Fukuoka 814-0180, Japan

Nuclear Science and Engineering Center, Japan Atomic Energy Agency, 2-4 Shirakata, Tokai, Naka, Ibaraki 319-1195, Japan

Centre for Astrophysics Research, Department of Physics, Astronomy and Mathematics, University of Hertfordshire, Hat eld, AL10 9AB, UK

Abstract

Received 2024 December 29; revised 2025 August 5; accepted 2025 August 19; published 2025 October 17

We present a potassium (K) abundance analysis in extremely metal-poor (EMP) stars based on high-resolution ($R \sim 60,000$) spectra obtained with the High Dispersion Spectrograph on the Subaru Telescope, covering the K I resonance lines at 766 and 769 nm. One-dimensional local thermodynamic equilibrium (LTE) abundances of K and other elements, including Na, Mg, Ca, Ti, Cr, and Ni, were derived using spectral synthesis. Non-LTE (NLTE) corrections were applied to the K abundances by interpolating a precomputed grid of corrections based on stellar parameters and the LTE K abundance. We detected K I lines in seven stars with [Fe/H] < -3.0 and derived upper limits for other stars in the same metallicity regime, making this sample well-suited for investigating the nucleosynthesis origins of K in the early Universe. We found that the [K/Fe] and [K/Ca] ratios of the seven stars are enhanced relative to the solar value, with a scatter of ~0.1 dex, as small as the typical measurement uncertainty. Under the assumption that each star formed from gas purely enriched by a single or a few massive star's supernova, the small scatter in [K/Fe] and [K/Ca], contrasted with the ~0.7 dex scatter in [Na/Mg] ratios (after NLTE correction), suggests that the production of K in massive stars or their supernovae is independent of the processes that drive the Na/Mg variation. These findings demonstrate that K abundances in EMP stars, and their correlations with other elemental abundances, can serve as sensitive tracers of the physical mechanisms governing the final evolutionary stages of massive stars and their supernova explosions.

Unified Astronomy Thesaurus concepts: Galactic archaeology (2178); Nucleosynthesis (1131); Late stellar evolution (911); Core-collapse supernovae (304)

Materials only available in the online version of record: machine-readable tables

1. Introduction

The origins of odd-atomic-numbered elements such as potassium (K, Z=19), scandium (Sc, Z=21), vanadium (V, Z=23), and manganese (Mn, Z=25) have been a topic of debate for many years, but no consensus has yet been obtained. The astrophysical origins of these elements are important not only because they are an essential ingredient for life on Earth, but also because they could serve as a tracer of extremely high temperature and density only realized in the deep cores of massive stars or at a brief moment of supernova explosions, which are impossible to directly observe.

Potassium (K) is a particularly important element because its yield is highly sensitive to various physical processes

Original content from this work may be used under the terms of the Creative Commons Attribution 4.0 licence. Any further distribution of this work must maintain attribution to the author(s) and the title of the work, journal citation and DOI.

associated with stellar and supernova nucleosynthesis. The dominant isotope of K, ³⁹K, is predicted to be synthesized by oxygen burning in the innermost regions of massive stars (e.g., S. E. Woosley & T. A. Weaver 1995). However, Galactic chemical evolution models that incorporate the K yields from one-dimensional nucleosynthesis calculations of the evolution and explosion of massive stars underproduce K abundances observed in stars by more than >1 dex (e.g., F. X. Timmes et al. 1995; Y. Takeda et al. 2009; S. M. Andrievsky et al. 2010; K. Nomoto et al. 2013; H. Reggiani et al. 2019; C. Kobayashi et al. 2020). Furthermore, in the old globular cluster NGC 2419, the most luminous globular cluster in the Milky Way's outer halo, an anticorrelation between K and Mg abundances has been reported (J. G. Cohen et al. 2011; A. Mucciarelli et al. 2012). The nucleosynthetic mechanism responsible for the synthesis of K that could account for this trend remains unclear.

Multidimensional effects in presupernova stellar evolution in massive stars have been suggested to enhance the production of odd-Z elements, including K. C. Ritter et al. (2018) used 3D hydrodynamic simulations to explore the nucleosynthesis resulting from the injection of C into the convective O-shell in the late evolution phase of massive stars

^{*} This research is based on data collected at the Subaru Telescope, which is operated by the National Astronomical Observatory of Japan. We are honored and grateful for the opportunity of observing the Universe from Maunakea, which has cultural, historical, and natural significance in Hawaii.

with $M=25~M_{\odot}$. Such C–O shell mergers are shown to explain the observed abundances of odd-Z elements in Galactic metal-poor stars. The occurrence of the shell merger in the final stage of massive stellar evolution is further supported by recent X-ray spectroscopy of young supernova remnants, which reveals spatial variations in elemental abundance ratios predicted by this mechanism (T. Sato et al. 2025).

Explosive nucleosynthesis that involves neutrino transport in core-collapse supernovae has also been proposed to be a possible production site of odd-Z elements, including K (e.g., T. Yoshida et al. 2008; C. Kobayashi et al. 2011). Explosive nucleosynthesis yields of odd-Z elements such as K, Sc, V, and Mn are generally sensitive to the proton-to-nucleon ratio, denoted as Y_e , in the innermost layers of the SN ejecta (N. Iwamoto et al. 2006). The distribution of Y_e in the innermost layers of SN ejecta is determined by the interaction of neutrinos with neutrons and protons, which ultimately affects the nucleosynthesis yields. This process also determines the heating of matter through neutrino transport, which helps facilitate a successful explosion. Indeed, while onedimensional simulations of core-collapse SNe fail to reach successful explosions (K. Sumiyoshi et al. 2005), multidimensional SN simulations indicate that a key to successful explosions is the mechanism involving those neutrino-heating processes (S. Wanajo et al. 2011; K. Kotake et al. 2012; T. Takiwaki et al. 2014; R. Bollig et al. 2021; D. Vartanyan et al. 2025; K. Nakamura et al. 2025). Nucleosynthesis yields of core-collapse supernovae based on multidimensional simulations with self-consistent treatment of neutrino transport confirmed that some of the odd-Z element isotopes are enhanced under the high Y_e environment realized in the simulation, which alleviates the discrepancy between the observed and predicted abundances of odd-Z elements (S. Wanajo et al. 2018; A. Sieverding et al. 2023; T. Wang & A. Burrows 2024).

Extremely metal-poor (EMP) stars provide a unique opportunity to independently test the nucleosynthesis yields of massive stars, since their surface composition is likely determined by only a few supernovae of the first generation of massive stars (e.g., J. Audouze & J. Silk 1995). The chemical abundance patterns of these stars, therefore, are an important probe of the late evolution of the cores of progenitor stars or the physical condition (e.g., temperature, density) of stellar and supernova nucleosynthesis (H. Umeda & K. Nomoto 2005; N. Tominaga et al. 2007; A. Heger & S. E. Woosley 2010; K. Takahashi et al. 2014; N. Tominaga et al. 2014; V. M. Placco et al. 2015; M. N. Ishigaki et al. 2018).

The main reason for the scarcity of the K abundance data for EMP stars is that the KI resonance lines at 766.49 and 769.99 nm, which are only useful K lines in optical wavelengths, are very weak in EMP stars (typical equivalent widths of ~10–30 mÅ) and thus observations with high signal-to-noise ratios (S/Ns) are required. In practice, such a sensitivity is feasible only with 8–10 m class telescopes for the majority of EMP stars. Furthermore, these lines frequently overlap with strong telluric absorption lines (e.g., O₂). The precise K abundance estimates in EMP stars, therefore, can only be achieved with a careful correction for the telluric absorption features. On top of that, the abundance estimates using the KI lines are known to be largely affected by nonthermodynamic equilibrium (NLTE) effects. Over the last decade, the number of known EMP stars has been

continuously increasing, resulting in a sample of more than >50 stars with [Fe/H] < -3.5. (e.g., W. Aoki et al. 2013; J. G. Cohen et al. 2013; D. Yong et al. 2013; I. U. Roederer et al. 2014; H. Li et al. 2022). In these studies, however, K abundances are only sparsely reported for EMP stars because of the difficulties mentioned above.

In this paper, we present a new analysis of high-resolution spectra of K I resonance lines of stars with [Fe/H] < -3.0. We derived [K/H] abundance ratios under the local thermodynamic equilibrium (LTE) assumption and then applied the NLTE correction on the basis of a published grid of corrections. We obtain an upper limit based on the observed spectra for stars whose K I lines are undetectable.

This paper is organized as follows. Section 2 describes sample selection and high-resolution spectroscopic observations. Section 3 provides details of the derivation of K abundances and their NLTE correction. Analysis of other elemental abundances is also described. Section 4 presents the resulting abundances and upper limits of K for the sample stars as well as their ratios with other elemental abundances. Section 5 compares observed abundances with theoretical yield models. Finally, the conclusion is given in Section 6.

2. Data

2.1. Observation

The sample stars were selected based on the studies by J. G. Cohen et al. (2013), D. Yong et al. (2013), I. U. Roederer et al. (2014), H. R. Jacobson et al. (2015), and E. Fernández-Alvar et al. (2016). These studies conducted high-resolution spectroscopic surveys of a large sample of EMP stars. Stars with V-band magnitude <15 are chosen as primary targets to ensure a high S/N near the K absorption lines at 766.49 and 769.896 nm.

Observations were carried out on 2016 November 12 and 13, and 2017 January 18, with a high-dispersity spectrograph at the Subaru Telescope (K. Noguchi et al. 2002). The standard setting, "StdRa," was used with a slit width of 0."6. This setting yields the wavelength coverage of 514–637 nm for the blue CCD and 657–778 nm for the red CCD with a spectral resolution of $R \sim 60,000$. An on-chip binning of 2×2 (spatial \times wavelength directions) was applied to maximize S/N without degrading the spectral resolution. In order to identify telluric absorption lines contaminating the target's spectra, we observed telluric standard stars frequently during the observing nights. Table 1 summarizes the coordinates, date of observation, total exposure time, and magnitudes of the target stars. The values of S/Ns per pixel estimated in the blue CCD and in the vicinity of the K I 766 and 769 nm lines are also presented.

Radial velocities were measured by cross-correlating the observed spectra of the blue CCD with the template spectra. The spectra taken by the red CCD were not used for the radial velocity estimate since the number of detectable metal absorption lines for the wavelength range covered by the red CCD is much smaller than that of the blue CCD. The estimated radial velocities and their uncertainties are listed in the last two columns of Table 1.

The S/N of one of the sample stars, HE 0130–1749, is below 20 around the wavelengths of both K I 766 and 769 nm lines, which is not sufficient to obtain useful abundance estimates. For HE 0132–2439, only a few Fe absorption lines

Table 1 Summary of the Observations

Name	R.A. (deg)	Decl. (deg)	Date	Exptime (s)	Gmag (mag)	SN_B	SN ₇₆₆	SN ₇₆₉	RV (km s ⁻¹)	$\sigma_{RV} \over (\text{km s}^{-1})$
CS 30339-0073	8.717	-36.924	12-11-2016	7200	14.5	22	25	22	162.95	0.45
CS 22942-0002	11.649	-24.715	12-11-2016	3600	13.7	37	41	33	-159.32	0.57
CD-38 245	11.65	-37.658	12-11-2016	1200	11.7	98	118	104	46.97	1.02
CD-30 298	14.683	-30.098	12-11-2016	600	10.6	120	131	115	28.75	0.15
HE 0130-1749	23.108	-17.572	18-01-2017	7200	14.6	16	17	14	-117.52	0.21
HE 0132-2439	23.745	-24.404	12-11-2016	7200	14.6	20	22	20	-19.03	0.22
BD+44 493	36.709	44.964	12-11-2016	600	8.9	130	143	118	-149.0	0.38
CS 22189-0009	40.427	-13.469	13-11-2016	5400	13.8	33	37	33	-20.57	0.37
CS 22963-0004	44.193	-4.855	13-11-2016	2700	14.8	38	38	34	293.54	0.35
CS 22172-0002	48.586	-10.585	13-11-2016	1800	12.5	72	82	74	252.12	0.42
HE 0344-0243	56.707	-2.569	18-01-2017	7200	14.9	19	20	17	-111.23	0.25
SMSS J085924.06-120104.9	134.849	-12.018	12-11-2016	8100	14.0	32	39	34	203.09	0.25
HE 0926-0546	142.366	-5.996	13-11-2016	8100	14.0	26	30	26	148.87	1.11
HE 1012-1540	153.722	-15.934	18-01-2017	7200	13.9	38	37	33	222.59	0.55
BS 16076-0006	192.094	20.944	18-01-2017	3600	13.3	36	35	30	206.3	0.39
BS 16929-0005	195.872	33.851	18-01-2017	4800	13.4	42	43	35	-52.17	0.36
SDSSJ134338.67+484426.6	205.911	48.739	18-01-2017	2700	12.0	111	106	85	-133.07	0.29
BS 16550-087	212.609	18.022	18-01-2017	4800	13.5	34	36	30	-148.95	0.29
CS 22950-0046	305.368	-13.275	13-11-2016	7200	13.9	25	32	28	107.33	0.31
CS 22949-0048	351.53	-5.834	13-11-2016	5400	13.4	47	56	46	-161.64	0.22

Note. Basic properties and observational details of the sample stars. The table presents the star names, coordinates in the ICRS, exposure times, G-band magnitudes, S/Ns for the blue CCD and at the wavelengths of the K I 766 nm and 769 nm lines, and the measured radial velocities (RV) and their uncertainties.

were detected to obtain a reliable metallicity estimate. We therefore exclude those two stars in the following analysis.

2.2. Data Reduction

The raw data were reduced by the software hdsql, ¹⁰ which utilizes standard IRAF routines (D. Tody 1993) together with the PyRAF package (Science Software Branch at STScI 2012). Using hdsql, we performed overscan subtraction, linearity correction, cosmic-ray rejection, scattered light subtraction, flat-fielding, aperture extraction, wavelength calibration, and heliocentric radial velocity correction.

Special care was taken for the two echelle orders that contained the K I lines on the red CCD. For those wavelengths, we divided the target spectrum by a standard star spectrum after shifting and rescaling it to minimize the difference between the two spectra in the vicinity of each of the K I lines. The spectra of standard stars were typically taken within a few hours of the observing time of a given target star. An IRAF routine "telluric" was used for this purpose.

3. Abundance Analysis

To perform the abundance analysis, we conducted line-byline spectral synthesis using the Turbospectrum code (B. Plez 2012) with the MARCS model atmospheres (B. Gustafsson et al. 2008) to fit the observed spectra. To automate the processes of interpolating the model atmosphere, generating synthetic spectra, and fitting the synthetic spectra, we utilized the iSpec python interface (S. Blanco-Cuaresma et al. 2014; S. Blanco-Cuaresma 2019).

3.1. Stellar Parameters

The stellar effective temperature ($T_{\rm eff}$), surface gravity (log g), metallicity ([Fe/H]), and microturbulence velocity ($v_{\rm mic}$) were obtained by the following steps:

- 1. An initial guess of [Fe/H] values was adopted from the literature.
- 2. $T_{\rm eff}$ was estimated based on Gaia DR3 and 2MASS photometry, taking into account the Galactic extinction at estimated distances of the sample stars.
- 3. $\log g$ was determined based on the absolute *G*-band magnitudes calculated based on an extinction-corrected *G*-band magnitude, the $T_{\rm eff}$ estimated by the step 1, and a stellar isochrone model.
- 4. Microturbulent velocities ($v_{\rm mic}$) were estimated using an empirical formula. Macroturbulent velocity was fixed to $4~{\rm km~s}^{-1}$ for red giant branch (RGB) stars and $2~{\rm km~s}^{-1}$ for the main-sequence star.
- 5. The [Fe/H] values were updated based on the Fe abundances from the spectra in this work by adopting the stellar parameters computed in the previous steps.

In Step 1, we adopted [Fe/H] values from high-resolution spectroscopic analyses of a large sample of very metal-poor stars by I. U. Roederer et al. (2014) when available, and supplemented these with values from other literature sources (see Table 2).

In Step 2, to accurately estimate the Galactic extinction along the lines of sight to the sample stars, we employed the three-dimensional dust map implemented in the dustmaps python package (G. Green 2018) to obtain E(B-V) values, incorporating the estimated distances from C. A. L. Bailer-Jones et al. (2021). For stars located at distances greater than 1 kpc or at Galactic latitudes $b > 60^{\circ}$, which are likely located beyond the bulk of the dust in the Galactic disk, we adopted

¹⁰ https://github.com/chimari/hds_iraf

Table 2
Stellar Parameters

Name	G (mag)	G_{BP} (mag)	G_{RP} (mag)	M_G (mag)	T _{eff} (K)	$\sigma_{T_{\rm eff}}$ (K)	log g (dex)	$\log g_{\text{low}}$ (dex)	$\log g_{\text{high}}$ (dex)	[Fe/H] (dex)	$\sigma_{ ext{[Fe/H]}}$ (dex)	T _{eff} (ini) (K)	$\log g(\text{ini})$ (dex)	[Fe/H](ini) (dex)	Ref
BS 16076-0006	13.3	13.7	12.8	2.4	5507	80	3.24	3.26	3.19	-3.34	0.03	5199	3.00	-3.81	B09
BS 16550-087	13.5	14.0	12.8	-1.1	4821	84	1.58	1.64	1.51	-3.34	0.01	4750	1.30	-3.39	C13
BS 16929-0005	13.4	13.8	12.9	1.1	5301	76	2.67	2.71	2.64	-3.22	0.01	5245	2.70	-3.34	L08
HE 1012-1540	13.9	14.2	13.3	5.7	5754	107	4.59	4.59	4.58	-3.22	0.03	5520	4.70	-3.51	C13
SDSSJ134338.67+484426.6	12.0	12.3	11.6	2.3	5853	80	3.32	3.32	3.31	-3.10	0.01	6030	3.34	-3.15	L21
BD+44 493	8.9	9.2	8.3	2.0	5388	82	3.17	3.17	3.16	-3.65	0.01	5040	2.10	-4.28	R14
CD-30 298	10.6	11.0	10.0	1.2	5332	76	2.67	2.68	2.65	-3.09	0.01	4810	1.50	-3.77	R14
CD-38 245	11.7	12.2	11.0	-1.3	4947	107	1.60	1.64	1.55	-3.81	0.01	4520	0.65	-4.59	R14
CS 22189-0009	13.8	14.2	13.2	0.2	5009	76	2.18	2.24	2.11	-3.26	0.01	4540	0.60	-3.92	R14
CS 22172-0002	12.5	12.9	11.8	-0.8	4945	94	1.75	1.81	1.69	-3.53	0.01	4800	1.30	-3.86	H13
CS 22942-0002	13.7	14.0	13.1	1.5	5398	71	2.89	2.94	2.84	-3.03	0.01	5010	2.00	-3.61	R14
CS 22949-0048	13.4	13.9	12.7	0.5	4876	64	2.25	2.31	2.20	-3.15	0.01	4620	0.95	-3.55	R14
CS 22950-0046	13.9	14.4	13.2	-1.1	4716	73	1.59	1.68	1.49	-3.45	0.01	4380	0.50	-4.12	R14
CS 22963-0004	14.8	15.1	14.3	1.7	5648	73	3.03	3.09	2.96	-3.03	0.02	5060	2.15	-4.09	R14
CS 30339-0073	14.5	14.9	14.0	1.7	5355	90	2.92	2.98	2.86	-3.16	0.02	4830	1.55	-3.93	R14
HE 0344-0243	14.9	15.4	14.3	0.2	5176	77	2.29	2.35	2.22	-3.00	0.03	5140	2.30	-3.35	C13
HE 0926-0546	14.0	14.4	13.4	0.3	5188	81	2.27	2.33	2.21	-3.55	0.02	5159	2.50	-3.73	C13
SMSS J085924.06-120104.9	14.0	14.6	13.3	-0.9	4671	81	1.65	1.73	1.59	-3.33	0.01	4459	1.20	-3.48	J15

Note. Stellar parameters derived in this study. G, $G_{\rm BP}$, and $G_{\rm RP}$ represent the apparent magnitudes in the Gaia passbands. M_G is the estimated absolute magnitude based on Gaia DR3 parallaxes. The uncertainty in $T_{\rm eff}$ reflects the calibration uncertainty from L. Casagrande et al. (2021). The values of $\log g_{\rm low}$ and $\log g_{\rm high}$ indicate the surface gravity estimates when parallaxes are varied within their reported uncertainties. The uncertainty in $[{\rm Fe/H}]$ includes only statistical errors.

(This table is available in machine-readable form in the online article.)

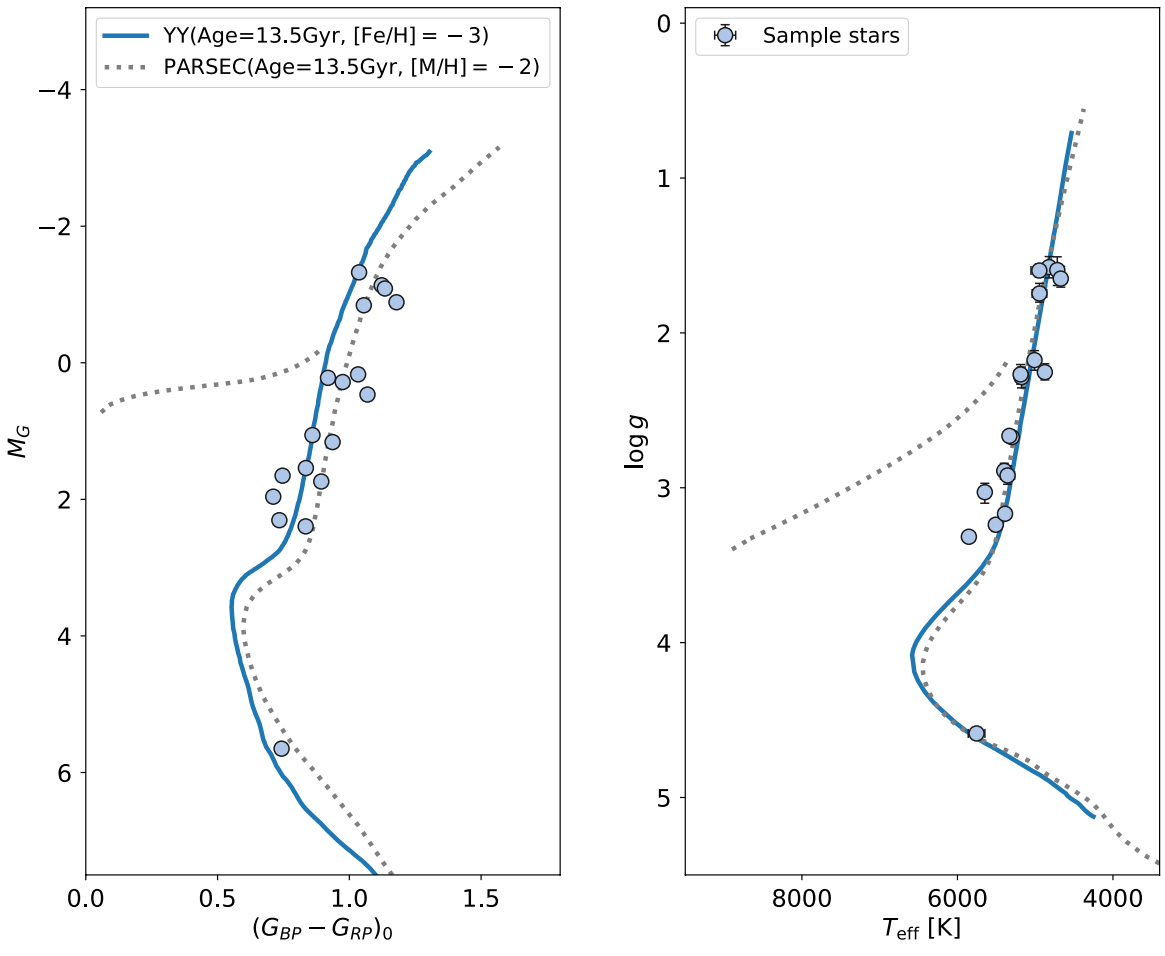


Figure 1. Left: color-magnitude diagram for the sample stars in the Gaia passbands (filled circles). The vertical axis shows absolute magnitude in G-band, and the horizontal axis shows extinction-corrected $G_{\rm BP}-G_{\rm RP}$ color. Right: adopted stellar parameters ($T_{\rm eff}$ and $\log g$) computed in this work. For both panels, the Y^2 isochrone model for an age of 13 Gyr and $[{\rm Fe}/{\rm H}]=-3$ used to derive $\log g$ is shown by the solid blue line. For comparison, the PARSEC isochrone for an old $(\log({\rm Age~yr}^{-1})=10.13)$ and metal-poor ($[{\rm M}/{\rm H}]=-2$) stellar population is shown as a dotted gray line.

extinction values from the two-dimensional dust map of E. F. Schlafly & D. P. Finkbeiner (2011). In all other cases, we used the three-dimensional dust map of G. M. Green et al. (2019). The estimated extinction values, together with Gaia DR3 and 2MASS photometry, were used to determine $T_{\rm eff}$ based on the color–temperature calibration of L. Casagrande et al. (2021), as implemented in the colte¹¹ package. The resulting uncertainties in $T_{\rm eff}$ range from 62 to 107 K.

In Step 3, we first estimated the extinction-corrected absolute G-band magnitude (M_G) and the $G_{\rm BP}-G_{\rm RP}$ color. The extinction values for the G, $G_{\rm BP}$, and $G_{\rm RP}$ bands were derived using the coefficients provided by N. F. Martin et al. (2024), based on the estimated E(B-V), $T_{\rm eff}$, and an initial guess of [Fe/H]. The left panel of Figure 1 displays the derived M_G and the extinction-corrected $G_{\rm BP}-G_{\rm RP}$ color. Bolometric magnitudes ($M_{\rm bol}$) were obtained by interpolating the Yonsei–Yale (Y^2) isochrones version 3 (P. Demarque et al. 2004; S. K. Yi et al. 2008) for an age of 13 Gyrs and [Fe/H] = -3, at the corresponding M_G . The solid blue line represents the Y^2 isochrone used for the interpolation. For comparison, the PARSEC isochrone for an old (log(Age/yr) = 10.13) and metal-poor ([M/H] = -2) stellar population is

shown as a dotted gray line (C. T. Nguyen et al. 2022). As shown in this figure, the majority of the sample stars are located on the red giant branch, while one star, HE 1012 -1540, lies on the main sequence.

Finally, we applied the fundamental relation from P. E. Nissen et al. (1997), using the estimated values of $M_{\rm bol}$ and $T_{\rm eff}$.

$$\log \frac{g}{g_{\odot}} = \log \frac{M}{M_{\odot}} + 4\log \frac{T_{\rm eff}}{T_{\rm eff}, \odot} + 0.4(M_{\rm bol} - M_{\rm bol, \odot}). (1)$$

The adopted solar values are $T_{\rm eff,\odot}=5777~{\rm K}$, $\log g_{\odot}=4.4$, and $M_{\rm bol,\odot}=4.71$. Stellar masses in Equation (1) are assumed to be $0.71 M_{\odot}$ for RGB stars and $0.66 M_{\odot}$ for main-sequence stars, which correspond to the median value of the isochrone model in the range $3 < M_G < -1$ (RGB) or $5 < M_G < 6$ (main sequence), respectively. The uncertainties in $\log g$ due to the uncertainty in the distance estimate given by C. A. L. Bailer-Jones et al. (2021) are 0.1 dex at most.

In Step 4, we adopted the empirical formula of J. A. Holtzman et al. (2018) to estimate the microturbulent velocity ($v_{\rm mic}$) based on the given values of log g and [Fe/H]. Minor adjustments were applied, when necessary, to best reproduce the observed absorption line profiles.

¹¹ https://github.com/casaluca/colte

Table 3
Atomic Line List

Element	Wavelength (nm)	Excp (eV)	log gf
		. ,	0.140
K 1	766.490	0.000	0.149
K 1	769.896	0.000	-0.154
Na 1	568.263	2.102	-0.706
Na 1	588.995	0.000	0.108
Na 1	589.592	0.000	-0.144
Na 1	615.423	2.102	-1.547
Na 1	616.075	2.104	-1.246
Mg 1	517.268	2.712	-0.450
Mg 1	518.360	2.717	-0.239

Note. Table 1 is published in its entirety in machine-readable format. A portion is shown here for guidance regarding its form and content.

(This table is available in machine-readable form in the online article.)

In Step 5, the adopted values of [Fe/H] were iteratively updated until convergence within 0.1 dex was achieved.

The right panel of Figure 1 shows $T_{\rm eff}$ and $\log g$ computed in this work. As can be seen, the adopted values of these stellar atmospheric parameters are approximately consistent with the adopted Y^2 isochrone model. The $\log g$ values estimated using the Y^2 and PARSEC isochrone models are consistent within 0.08 dex.

3.2. Atomic Data

The adopted atomic data for K I and other metal absorption lines is shown in Table 3.

For elements other than K, we compile a line list suitable for extremely metal-poor stars and cover the spectral range of our observational setup from M. N. Ishigaki et al. (2012, 2013). We supplement the lines from D. Yong et al. (2013) to optimize the line selection for extremely metal-poor stars. We estimate the abundance of Na, Mg, Ca, Ti, Cr, Fe, and Ni, while the lines of Si, Sc, Mn, Co, Y, and Ba were too weak in the wavelength range covered in this work. We report the results of Na, Mg, Ca, Ti, Cr, Fe, and Ni in the following sections. The atomic data were adopted from version 6 of the Gaia-ESO line list, compiled by U. Heiter et al. (2021). Those data are based on various literature sources and the VALD¹² database (N. E. Piskunov et al. 1995; F. Kupka et al. 1999; T. Ryabchikova et al. 2015).

3.3. Metallicity

Figure 2 compares the values of [Fe/H] obtained in this work and those from the literature from which the initial guesses of [Fe/H] values were adopted (see Table 2). The [Fe/H] values estimated in this work are systematically higher than those derived in previous studies, sometimes by more than 0.5 dex. In particular, for nine stars analyzed in common with I. U. Roederer et al. (2014), the differences reach up to 1.0 dex. The differences in [Fe/H] estimates are mainly attributed to differences in the temperature scales adopted in this work and in the literature, where I. U. Roederer et al. (2014) used Fe I lines to derive $T_{\rm eff}$ by requiring the Fe abundances to not show a trend with the excitation potentials. The log g value was then derived using the Y^2 isochrone model (P. Demarque et al.

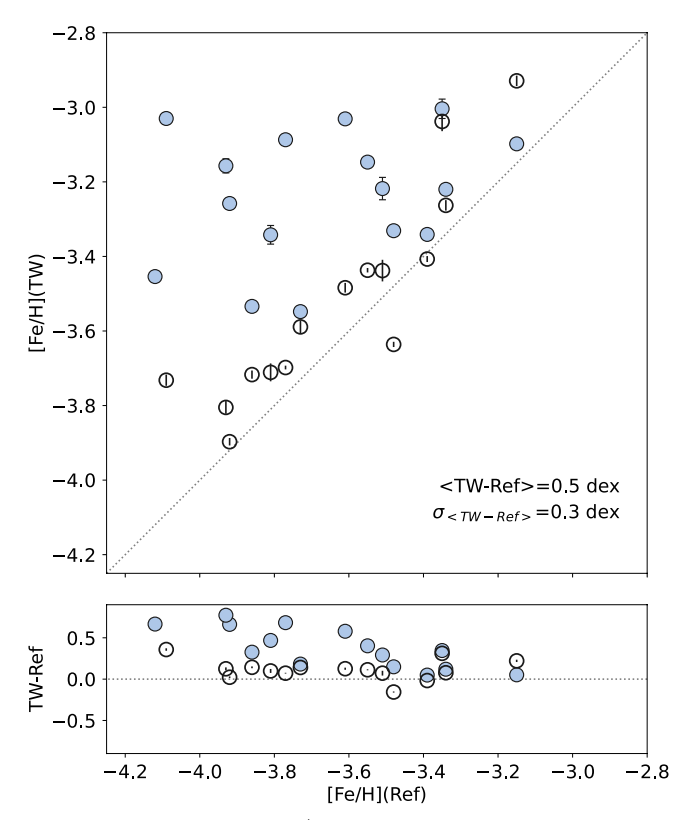


Figure 2. The comparison of [Fe/H] values derived in this work (the vertical axis) plotted against [Fe/H] values from the literature (the horizontal axis). Filled blue circles correspond to the values obtained by adopting $T_{\rm eff}$ and $\log g$ in this work. Open gray circles correspond to the values obtained by adopting the stellar parameters from the literature listed in Table 2.

2004). For CD–38 245 as an example, I. U. Roederer et al. (2014) obtained $T_{\rm eff}=4520\,\rm K$, $\log g=0.65$, and $[\rm Fe/H]=-4.59$. In contrast, this study obtained $T_{\rm eff}=4947\,\rm K$, $\log g=1.60$, and $[\rm Fe/H]=-3.82$. In the former case, $\log g$ is incompatible with the distance estimate of $d=3710\,\rm pc$ from C. A. L. Bailer-Jones et al. (2021). The gray open circles in Figure 2 show the $[\rm Fe/H]$ values estimated in this work when the same values of $T_{\rm eff}$ and $\log g$ were adopted in the abundance analysis. The agreement is significantly improved in this case.

To ensure homogeneity in the method by which the values of $T_{\rm eff}$, $\log g$, and [Fe/H] are derived, we adopted these parameters from this work in the following analysis. We address the consistency between the abundance ratios derived in this work and those from the literature in Section 3.5.

3.4. Potassium

Figure 3 presents examples of observed spectra before and after correcting for the telluric absorptions using the standard star spectra. The top two panels show the K I lines at 766.49 and 769.90 nm, respectively, for one of the sample stars. The bottom-left panel shows the K I line at 766.49 nm for a star with lower metallicity. As demonstrated in these examples, the dominant contribution from telluric lines was successfully removed when the telluric features were offset from the K I lines. Measurements were excluded when a K I line significantly overlapped with telluric absorption. The bottom-right panel illustrates a case in which only an upper limit on the potassium abundance could be derived.

¹² vald.astro.uu.se

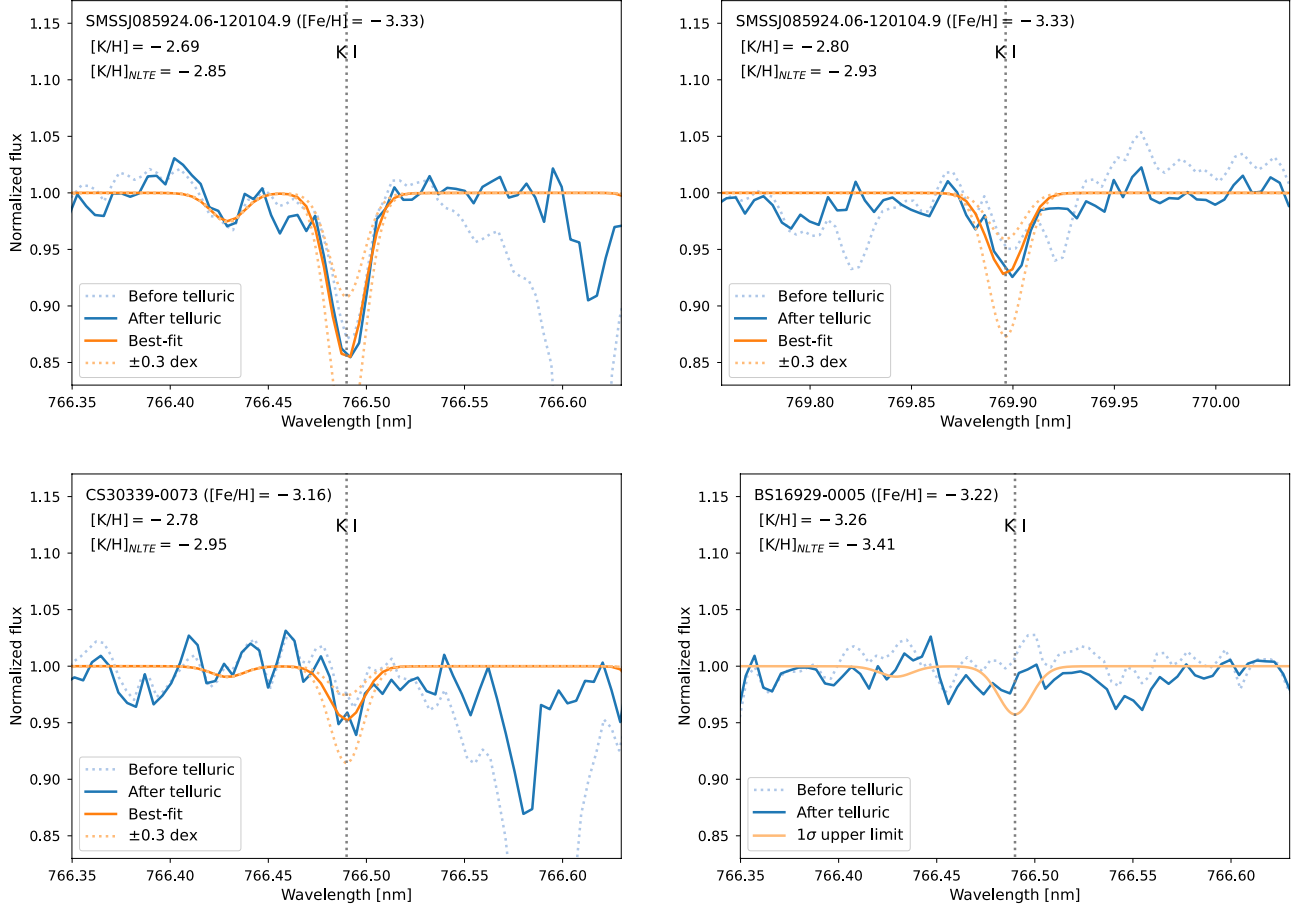


Figure 3. Observed and synthetic spectra of the K I lines. The light blue and deep blue solid lines represent the observed spectra before and after telluric correction, respectively. The solid orange lines indicate the best-fit synthetic spectra or the upper limit. The dotted orange lines show synthetic spectra with K abundances varied by 1σ . The top two panels display the two K I lines for SMSS J085924.06–120104.9. The bottom-left panel shows the spectrum of the lower-metallicity star CS 30339–0073. The bottom-right panel shows the case of BS 16929–0005, for which only an upper limit on the K abundance could be determined.

3.4.1. Synthetic Spectral Fitting

We fitted synthetic spectra to the observed spectra after normalizing the local continuum. The best-fit spectrum for a representative case is shown in Figure 3. We detected the KI 766.49 nm line in five of the sample stars and the 769.90 nm line in five of the sample stars. If the detection of the K I line is deemed uncertain based on visual inspection, we report only upper limits. Uncertainties on K abundances were estimated by performing 100 iterations of K abundance measurements using noise-added best-fit synthetic spectra, simulating the statistical fluctuations of the observed spectra at a given S/N. Similarly, the 1σ upper limits on K abundances were estimated by performing the measurements using line-free synthetic spectra. The sum of the mean K abundance derived from line-free spectra and the corresponding 1σ scatter is reported as the value of 1σ upper limit. An example synthetic spectrum corresponding to the 1σ upper limit is shown in the bottomright panel of Figure 3.

3.4.2. NLTE Correction

Both K I lines used in this study are known to be sensitive to deviations from LTE (Y. Takeda et al. 2002; S. M. Andrievsky et al. 2010; G. Zhao et al. 2016; H. Reggiani et al. 2019). We used the grid of NLTE corrections for the K I 766.49/769.90 nm lines calculated by H. Reggiani et al. (2019). The

grid is interpolated to obtain corrections appropriate for each sample star based on its estimated values of $T_{\rm eff}$, log g, [Fe/H], $v_{\rm mic}$, and [K/Fe].

3.5. Other Elements

The same spectral fitting technique described in Section 3.4.1 was used to determine the abundances of Na, Mg, Ca, Cr, Ti, and Ni. Only a small number of stars exhibit measurable absorption lines for additional elements (e.g., Al, Mn, Zn, etc.), primarily due to the redder wavelength coverage of the spectra analyzed in this study. To better constrain the nucleosynthetic yield models that account for the overall abundance patterns of the sample stars (see Section 5.2), we supplemented the abundance estimates of Sc, V, and Mn using values from I. U. Roederer et al. (2014), H. R. Jacobson et al. (2015), and D. K. Lai et al. (2008).

Figure 4 compares the [Mg/Fe], [Ca/Fe], and [Ni/Fe] ratios obtained in this work and those from the literature (Table 2). Despite the large difference in the adopted [Fe/H] values (see Figure 2), the mean offsets of the abundance ratios are up to 0.19 dex. The mean offset of -0.15 dex in the [Ni/Fe] ratios is significantly larger than the standard deviation of the differences. The discrepancy between the Ni abundances estimated in this work and those from I. U. Roederer et al. (2014), which are primarily adopted as literature values, is likely due to the different sets of Ni I lines used. While

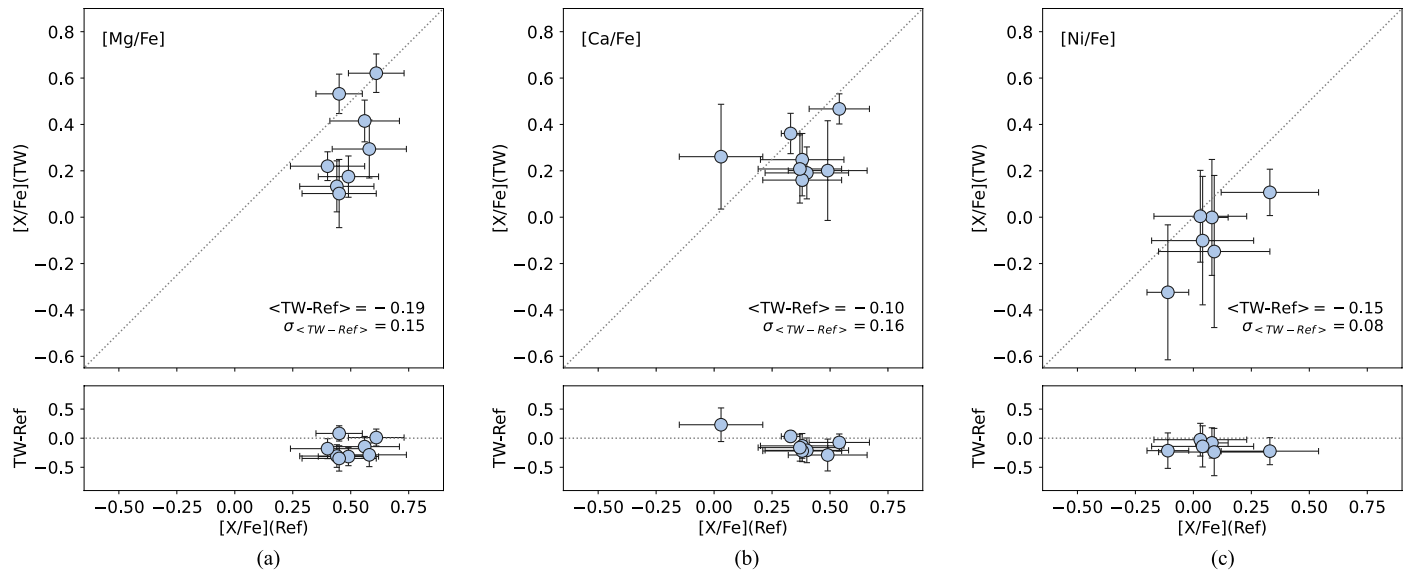


Figure 4. The comparison of (a) [Mg/Fe], (b) [Ca/Fe], and (c) [Ni/Fe] ratios derived in this work (the vertical axis) plotted against corresponding values from the literature listed in Table 2 (the horizontal axis).

I. U. Roederer et al. (2014) mainly used lines at shorter wavelengths (<500 nm), this study utilizes lines at longer wavelengths. In I. U. Roederer et al. (2014), one Ni I line at 547.7 nm, which is commonly analyzed in both studies, yields lower Ni abundances compared to those derived from the shorter-wavelength lines. This systematic difference does not directly affect the main conclusions of this work.

4. Result

4.1. [K/Fe], [K/Ca] Ratios

Among the 18 stars analyzed, K abundances were estimated for seven stars based on at least one of the K I lines. For the other 11 objects, only a 1σ upper limit could be determined. The K abundances derived are summarized in Table 4.

The resulting [K/Fe] values from the LTE analysis are shown in the top-left panel of Figure 5. For the seven stars with measured [K/Fe] abundances, the values range from 0.3 to 0.7 dex, with a mean of 0.51 dex and a standard deviation of 0.13 dex. This dispersion is smaller than the typical statistical uncertainty in the measured [K/Fe] abundances (approximately 0.2 dex). The upper limits obtained for the remaining stars are consistent with the 2σ range of the measured abundances. For comparison, LTE abundances from R. Cayrel et al. (2004) are also plotted in the same panel. The [K/Fe] ratios derived in this study are in good agreement with those reported by R. Cayrel et al. (2004).

The top-right panel of Figure 5 shows the [K/Fe] ratios after applying the NLTE corrections based on the calculations by H. Reggiani et al. (2019). The mean [K/Fe] value is 0.35 dex, which is lower than the LTE result by 0.16 dex. The standard deviation remains 0.13 dex, again less than the typical statistical uncertainty. It should be noted that systematic uncertainties associated with the NLTE corrections are not included in this analysis. For comparison, NLTE K abundances from Y. Takeda et al. (2009), based on a reanalysis of the R. Cayrel et al. (2004) sample, are also shown. The [K/Fe] ratios derived in this study are consistent with the supersolar values and small scatter observed in the sample of Y. Takeda

et al. (2009) and H. Reggiani et al. (2019). The low upper limit for CD–38 245 at [Fe/H] = -3.8 is consistent with the slightly decreasing trend of $[K/Fe]_{NLTE}$ seen in the sample of Y. Takeda et al. (2009).

The two bottom panels of Figure 5 present the [K/Ca] and $[K/Ca]_{NLTE}$ ratios derived from LTE and NLTE analyses, plotted as a function of [Ca/H]. Using Ca as the reference element instead of Fe provides a clearer insight into the condition of K nucleosynthesis, as both elements originate from similar layers within the progenitor star before and after the core-collapse supernova explosion. For the stars with detected K lines, the mean $[K/Ca]_{NLTE}$ ratio is 0.11 dex, with a scatter of 0.12 dex.

4.2. Abundance Ratios of Other Elements [X/Fe]

Table 5 summarizes the abundances of Na, Mg, Ca, Ti, Cr, and Ni derived from our analysis. Figure 6 presents the corresponding abundance ratios as a function of [Fe/H]. For comparison, the values obtained by R. Cayrel et al. (2004) are shown. The [X/Fe] trends with respect to [Fe/H], as obtained in this work, are in good agreement with those of R. Cayrel et al. (2004). The Ni abundance ratios shown in the bottom-right panel exhibit a hint of systematic offset at the lowest metallicities. This is likely due to the different Ni I lines adopted in R. Cayrel et al. (2004), for the same reason discussed in Section 3.5.

4.3. Abundance Patterns

Figure 7 presents the abundance patterns of stars with estimated $[K/Fe]_{\rm NLTE}$ ratios for Na, Mg, K, Ca, Ti, Cr, and Ni, as determined in this study. For reference, the abundances of C and N are adopted from H. R. Jacobson et al. (2015) for SMSS J085924.06–120104.9 and from I. U. Roederer et al. (2014) for the other stars. None of those stars exhibit enhancements in Sr, Y, or Ba above solar values (I. U. Roederer et al. 2014; H. R. Jacobson et al. 2015), and thus these elements are not shown in the figure.

Table 4
K Abundances

Name	[Fe/H] (dex)	[Ca/H] (dex)		[K/H] ₇₆₆ (dex)	$\Delta_{\text{NLTE,766}}$ (dex)		[K/H] ₇₆₉ (dex)	$\Delta_{\text{NLTE,769}}$ (dex)		[K/Fe] (dex)	e[K/Fe] (dex)	[K/Fe] _{NLTE} (dex)
CS 22189-0009	-3.26	-3.02					-2.83	-0.15		0.42	0.16	0.28
CS 22942-0002	-3.03	-2.84		-2.43	-0.19	<	-2.57	-0.17		0.60	0.09	0.41
CS 22172-0002	-3.53	-3.27					-2.83	-0.15		0.70	0.09	0.56
SMSS J085924.06-120104.9	-3.33	-2.87		-2.69	-0.16		-2.80	-0.13		0.61	0.06	0.46
CS 30339-0073	-3.16	-2.96		-2.78	-0.16					0.37	0.20	0.21
CS 22950-0046	-3.45	-3.25		-2.90	-0.14		-2.99	-0.13		0.53	0.09	0.39
CS 22949-0048	-3.15	-2.98		-2.83	-0.15		-2.83	-0.14		0.32	0.06	0.17
BS 16929-0005	-3.22	-2.86	<	-3.26	-0.15				<	0.25	0.29	0.10
BS 16550-087	-3.34	-3.03				<	-3.42	-0.12	<	0.19	0.27	0.07
BS 16076-0006	-3.34	-3.44				<	-3.18	-0.15	<	0.42	0.25	0.27
HE 1012-1540	-3.22	-2.98	<	-3.00		<	-2.40		<	0.54	0.33	
CD-38 245	-3.81	-3.51	<	-3.50	-0.13	<	-3.22	-0.13	<	0.42	0.11	0.29
SDSSJ134338.67+484426.6	-3.10	-3.09				<	-2.54	-0.22	<	0.68	0.12	0.46
BD+44 493	-3.65	-3.52	<	-3.03	-0.15	<	-3.22	-0.15	<	0.61	0.18	0.47
CD-30 298	-3.09	-2.94				<	-2.89	-0.16	<	0.30	0.10	0.15
CS 22963-0004	-3.03	-2.57	<	-2.54	-0.25				<	0.61	0.13	0.37
HE 0132-2439	-2.52	-2.64				<	-2.77	-0.16	<	0.01	0.32	-0.15
HE 0344-0243	-3.00	-2.69	<	-3.05	-0.15				<	0.28	0.33	0.12
HE 0926-0546	-3.55	-3.06	<	-2.80	-0.16	<	-2.91	-0.15	<	0.87	0.24	0.72

Note. Measured [Fe/H], [Ca/H], and [K/H] abundances in the sample stars. Measurements or upper limits are shown for each of the K I lines. Δ_{NLTE} indicates the non-LTE correction computed by interpolating the grid of H. Reggiani et al. (2019).

(This table is available in machine-readable form in the online article.)

As discussed in Section 4.1, the scatter in the $[K/Fe]_{NLTE}$ and $[K/Ca]_{NLTE}$ ratios are relatively low, estimated at \sim 0.1 dex. In contrast, the [Na/Fe] ratios show a larger scatter of 0.34 dex. When Mg is used as a reference element, the scatter in [Na/Mg] is as large as 1.45 dex. The scatter is partly caused by NLTE effects on Na and Mn abundances (I. Koutsouridou et al. 2025, and reference therein). After correcting for the NLTE effects by using the NillTE code provided by I. Koutsouridou et al. (2025) using the grid of K. Lind et al. (2022), the scatter in $[Na/Mg]_{NLTE}$ ratios is reduced to 0.74 dex. The value of the scatter in the $[Na/Mg]_{NLTE}$ ratios, however, remains large compared to the scatter in $[K/Ca]_{NLTE}$ ratios.

SMSS J085924.06–120104.9 displays a particularly high [Na/Fe] ratio of 0.62 dex and [Na/Fe]_{NLTE} = 0.20 dex, which largely contributes to the observed scatter. The star also exhibits the lowest [C/Fe] ratio among those with a detected K I line. The low [C/Fe] is likely due to stellar internal mixing, as the evolutionary correction of the carbon abundance proposed by V. M. Placco et al. (2014) can be as large as 0.4 dex for a star with $\log g = 1.65$ and [Fe/H] = -3.3. In contrast to carbon, the observed Na abundance likely reflects the star's initial composition, since Na is not expected to be affected by internal mixing processes.

For BS 16929–0005 (gray symbols in Figure 7), we obtained a relatively low upper limit for the K abundance. This star has previously been reported to be carbon enhanced, with [C/Fe] = 1.08 by W. Aoki et al. (2007), and a similar value of [C/Fe] = 0.97 by D. K. Lai et al. (2008).

The implications of these findings are discussed further in Section 5.1.

4.4. Correlation with Other Odd-Z Elements

To explore potential correlations between the estimated potassium abundances (K) and those of other odd-Z elements,

the left panels of Figure 8 present the abundance ratios [Sc/Fe], [V/Fe], and [Mn/Fe], adopted from I. U. Roederer et al. (2014), H. R. Jacobson et al. (2015), and D. K. Lai et al. (2008), respectively, plotted against the $[K/Fe]_{NLTE}$ ratios derived in this study.

The [Sc/Fe] and [V/Fe] ratios (top-left and middle-left panels) appear to be relatively consistent among the stars with measured K abundances. In contrast, the [Mn/Fe] ratio (bottom-left panel) exhibits a possible anticorrelation with [K/Fe]_{NLTE}. However, the weighted correlation coefficient of -0.99 is not statistically significant, as indicated by a p-value of 0.59, calculated from 1000 bootstrap resamplings of the abundance data. Neither the [K/Fe] nor [Mn/Fe] ratios show correlation with the values of $T_{\rm eff}$ or $\log g$, and thus the anticorrelation is unlikely to be caused by NLTE corrections on Mn abundances of stars with different stellar parameters. As a reference, the bottom-left panel of Figure 8 also shows the [Mn/Fe] ratios derived using Mn II lines by I. U. Roederer et al. (2014), which are known to be less affected by the NLTE effects (M. Bergemann et al. 2019), for four of the sample stars. The anticorrelation remains unchanged when using only those four stars.

A comparison between these observational results and theoretical predictions from stellar and supernova yield models is presented in Section 5.

5. Discussion

The K abundances estimated for EMP stars, including stars with [Fe/H] < -3.5, provide important insights into the nucleosynthetic yields from individual massive stars (A. Heger & S. E. Woosley 2010; K. Nomoto et al. 2013; N. Tominaga et al. 2014). Our new analysis of high-resolution spectra confirmed the previously reported supersolar values of the [K/Fe] ratios in the lowest [Fe/H] regimes (R. Cayrel et al. 2004; Y. Takeda et al. 2009; S. M. Andrievsky et al.

THE ASTROPHYSICAL JOURNAL, 992:215 (17pp), 2025 October 20

Table 5Derived Abundances of Fe, Na, Mg, Ca, Ti, Cr, and Ni

Name -	[Fe/H] (dex)	$\sigma_{ ext{[Fe/H]}}$ (dex)	[Na/Fe] (dex)	$\sigma_{ m [Na/Fe]} \ m (dex)$	[Mg/Fe] (dex)	$\sigma_{[\mathrm{Mg/Fe}]}$ (dex)	[Ca/Fe] (dex)	$\sigma_{ ext{[Ca/Fe]}} \ ext{(dex)}$	[Ti/Fe] (dex)	$\sigma_{ ext{[Ti/Fe]}}$ (dex)	[Cr/Fe] (dex)	$\sigma_{ ext{[Cr/Fe]}}$ (dex)	[Ni/Fe] (dex)	$\sigma_{ m [Ni/Fe]}$ (dex)
BS 16076-0006	-3.34	0.03	0.53	0.15	0.59	0.10	•••		•••	•••	-0.41	0.33	•••	•••
BS 16550-087	-3.34	0.01	-0.03	0.14	0.69	0.09	0.31	0.09	0.17	0.07	-0.46	0.09	-0.24	0.22
BS 16929-0005	-3.22	0.01	0.03	0.12	0.53	0.09	0.36	0.09	0.48	0.09	-0.22	0.14	-0.00	0.25
HE 1012-1540	-3.22	0.03	1.43	0.09	1.26	0.17		•••						•••
SDSSJ134338.67+484426.6	-3.10	0.01	-0.48	0.08	-0.43	0.08	•••	•••	0.64	0.39	-0.32	0.49	-0.10	0.35
BD+44 493	-3.65	0.01	0.16	0.06	0.62	0.05	0.15	0.20	0.34	0.25	-0.43	0.24		•••
CD-30 298	-3.09	0.01	-0.12	0.07	0.18	0.06	0.15	0.11	-0.03	0.12	-0.35	0.06	0.36	0.09
CD-38 245	-3.81	0.01	-0.19	0.07	0.17	0.07	0.33	0.25	0.21	0.11	-0.07	0.11		•••
CS 22189-0009	-3.26	0.01	-0.32	0.13	0.13	0.11	0.25	0.11	0.23	0.08	-0.24	0.10	0.00	0.20
CS 22172-0002	-3.53	0.01	-0.45	0.07	0.17	0.09	0.26	0.23	0.17	0.17	-0.53	0.13	-0.15	0.33
CS 22942-0002	-3.03	0.01	-0.01	0.13	0.41	0.09	0.19	0.11	0.37	0.11	-0.41	0.15	-0.10	0.28
CS 22949-0048	-3.15	0.01	0.16	0.12	0.22	0.06	0.16	0.07	0.48	0.04	-0.22	0.08	0.11	0.10
CS 22950-0046	-3.45	0.01	-0.28	0.14	0.29	0.12	0.20	0.21	0.13	0.12	-0.51	0.18		
CS 22963-0004	-3.03	0.02	0.66	0.12	0.22	0.12	0.46	0.13						•••
CS 30339-0073	-3.16	0.02	-0.09	0.16	0.10	0.15	0.21	0.15	0.56	0.14	-0.31	0.20		
HE 0130-1749	-3.08	0.02	0.17	0.23	0.71	0.17	0.60	0.17	0.32	0.22	-0.18	0.29	0.04	0.49
HE 0132-2439	-2.52	0.19	-1.20	0.37										
HE 0344-0243	-3.00	0.03	0.15	0.21	0.13	0.21	0.30	0.15	0.34	0.39	-0.55	0.27	0.67	0.42
HE 0926-0546	-3.55	0.02	0.33	0.16	0.35	0.14			0.83	0.27				
SMSS J085924.06-120104.9	-3.33	0.01	0.63	0.14	0.62	0.08	0.47	0.07	0.31	0.05	-0.50	0.09	-0.32	0.29

Note. Elemental abundance ratios of Fe, Na, Mg, Ca, Ti, Cr, and Ni for the sample stars. Statistical uncertainties are also shown.

(This table is available in machine-readable form in the online article.)

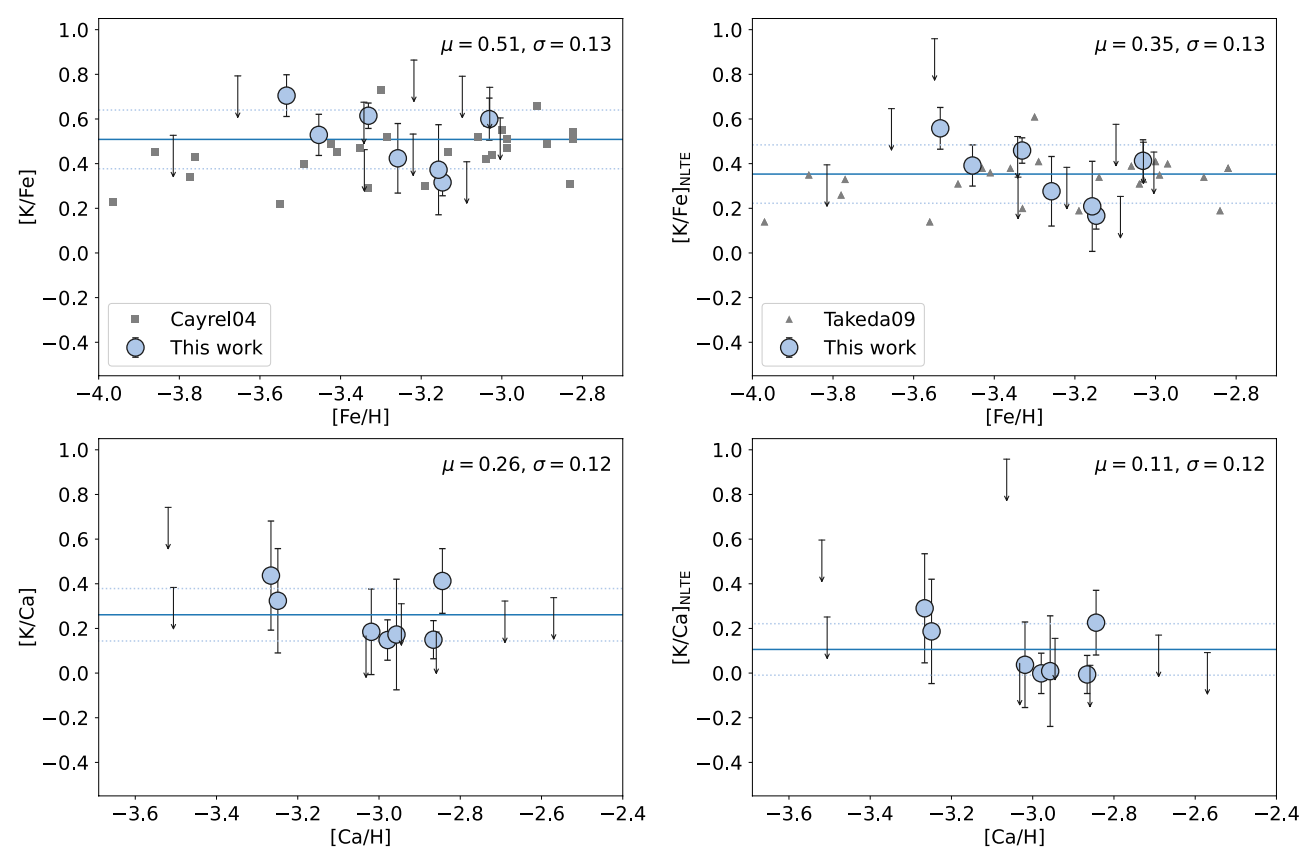


Figure 5. [K/Fe] and [K/Ca] ratios from the LTE (left panels) and NLTE (right panels) analysis obtained in this work. The stars with detected K I line(s) are shown by circles with error bars. The stars with only an upper limit are shown by arrows, where the location of the hats indicates 1σ of, essentially, the noise spectrum. For comparison, the abundances derived by R. Cayrel et al. (2004) and Y. Takeda et al. (2009) are shown by gray squares and triangles, respectively. Horizontal lines show the mean and the standard deviation of the abundance ratios for the stars with detected K I lines.

2010; H. Reggiani et al. 2019). Almost all of the stars studied in this work show enhancements not greater than $[K/Fe]_{NLTE} = 0.7$ dex. We also obtained a constraint on the scatter in the [K/Fe] and [K/Ca] ratios for stars with detected K lines.

5.1. Scatter in [Na/Mg] Ratios

Among the seven stars with measured K abundances, we found a significant scatter in the [Na/Mg] ratios. This scatter is unlikely to be caused by internal mixing processes, as neither Na nor Mg is expected to be altered at the stellar surface during the evolutionary stages of these stars. Therefore, the observed variation likely reflects inhomogeneities in the metalenriched gas from which the stars formed. Sodium and magnesium are synthesized during hydrostatic burning in massive stars, and their relative abundances are sensitive to the progenitor star's mass. In addition, Na production is influenced by the progenitor's metallicity and rotational velocities (e.g., K. Nomoto et al. 2013). Assuming that the abundance patterns observed in each star purely reflect the yield of a single supernova of a first-generation (Population III) star with the mass of 10-30 M_{\odot} , the scatter in [Na/Mg] ratios could be attributed to variations in progenitor properties such as mass, metallicity, and rotation. In contrast, the apparent coproduction of K and Ca, evidenced by the lack of scatter in [K/Ca] ratios, suggests that the yields of these elements are less sensitive to such progenitor characteristics.

5.2. Astrophysical Origins of K

Regarding the origin of K in the extremely metal-poor regime, two potential production sites have been proposed: (1) the final evolutionary stages of massive stars and (2) explosive nucleosynthesis during core-collapse supernovae. In the following subsections, we examine these scenarios in light of our abundance estimates.

5.2.1. The Final Stages of Massive Star Evolution

Hydrostatic oxygen burning in massive stars, which takes place during the final evolutionary stages of such stars, has been proposed as a potential site for K production (S. E. Woosley & T. A. Weaver 1995; S. E. Woosley et al. 2002). In particular, nucleosynthesis processes unique to rotating massive stars are predicted to enhance the yields of odd-Z elements, including K (M. Limongi & A. Chieffi 2018; L. Roberti et al. 2024). Chemical evolution models that incorporate yields from rotating massive stars are able to reproduce the observed [K/Fe] ratios, at least at low [Fe/H] regime (N. Prantzos et al. 2018; H. Reggiani et al. 2019).

To examine the scenario in which oxygen burning during the evolution of rotating massive stars serves as a dominant source of K in the observed EMP stars, Figure 9 presents the [K/Ca] ratios predicted by the one-dimensional stellar evolution and core-collapse supernova yield models of M. Limongi & A. Chieffi (2018). These models incorporate rotational mixing within the interiors of massive stars with initial masses ranging from 13 to $120M_{\odot}$. Different symbol

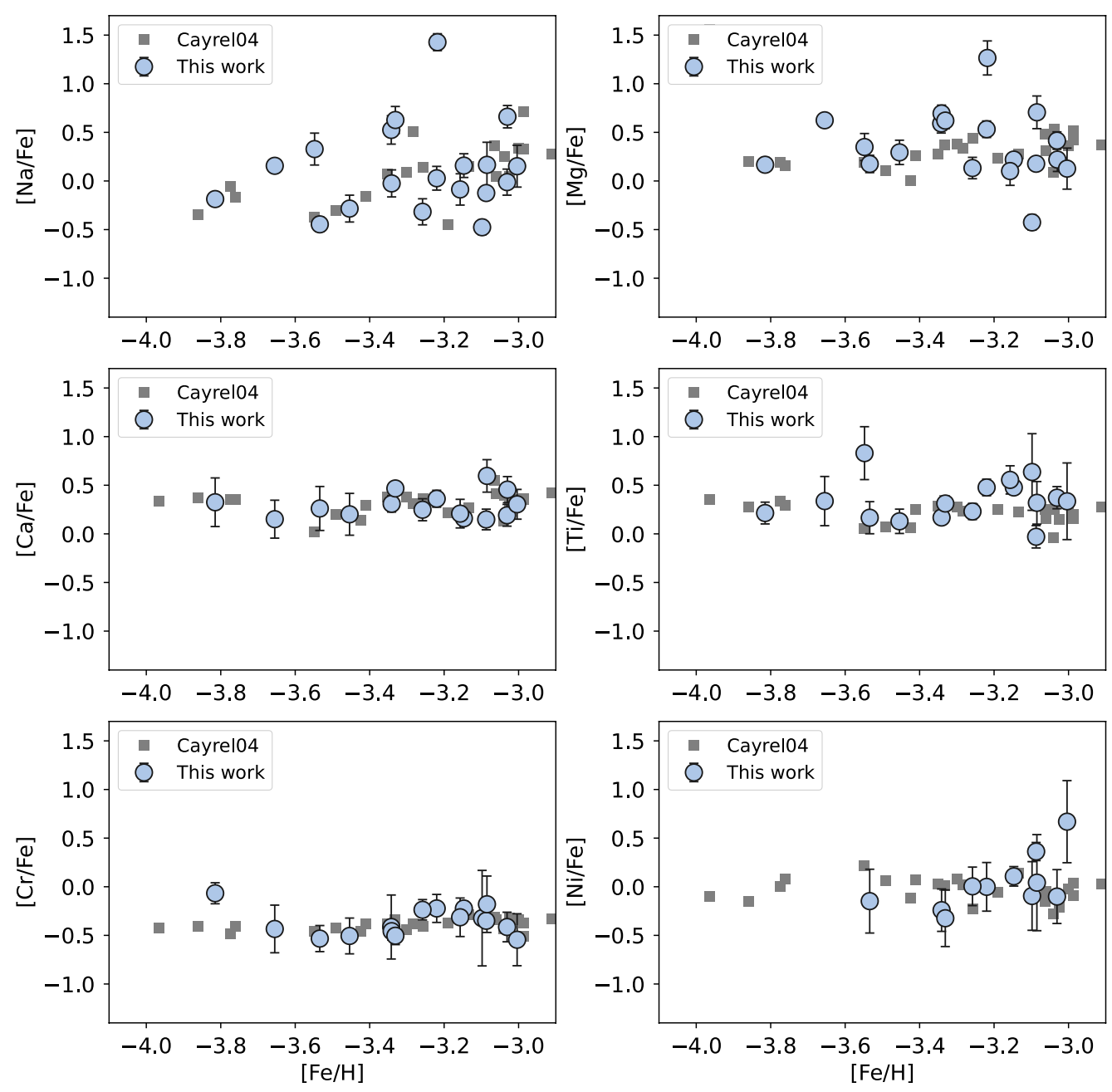


Figure 6. Abundances of other elements measured in this work. The gray squares show the results from R. Cayrel et al. (2004).

sizes represent models with progenitor masses of 13, 15, 20, and $25~M_{\odot}$ at [Fe/H] = -3.0, while different colors indicate initial rotational velocities of $V_{\rm rot}$ = 0, 150, 300 km s⁻¹. The models assume mixing below the base of the oxygen-burning shell and the ejection of 0.07 M_{\odot} of ⁵⁶Ni ("set R"). Stars with initial masses greater than 25 M_{\odot} are assumed to undergo a direct collapse into black holes, thereby not contributing to chemical enrichment. The observed 1σ and 2σ ranges of the [K/Ca] ratios derived in this study are indicated by dark and light gray shaded regions, respectively.

Among these models considered, the one with a progenitor mass of 15 M_{\odot} and a rotational velocity of $V_{\rm rot} = 300 \, {\rm km \, s}^{-1}$ (green triangles) shows the best agreement with the observed [K/Ca] ratios. The model with the same progenitor mass but a lower rotational velocity of $V_{\rm rot} = 150 \, {\rm km \, s}^{-1}$ (orange

triangles) is reasonably consistent with the observations within the 2σ range. In contrast, models with lower ($M=13M_{\odot}$) and higher ($M \ge 20M_{\odot}$) progenitor masses predict significantly lower [K/Ca] ratios, by $\gtrsim 0.5$ dex. Furthermore, nonrotating models (blue triangles) systematically yield lower [K/Ca] ratios across all considered masses by $\gtrsim 0.5$ dex.

The right panels of Figure 8 show the abundance ratios of [Sc/Fe], [V/Fe], and [Mn/Fe] plotted against [K/Fe], as predicted by the rotating massive star yield models of M. Limongi & A. Chieffi (2018). As in Figure 9, different colors indicate models with different initial rotational velocities ($V_{\rm rot}$). Similar to the trends seen in the [K/Ca] ratios, the model with a progenitor mass of 15 M_{\odot} and $V_{\rm rot} = 300\,{\rm km\,s^{-1}}$ (green triangles) predicts the highest abundances for K, Sc, V, and Mn. However, in contrast to

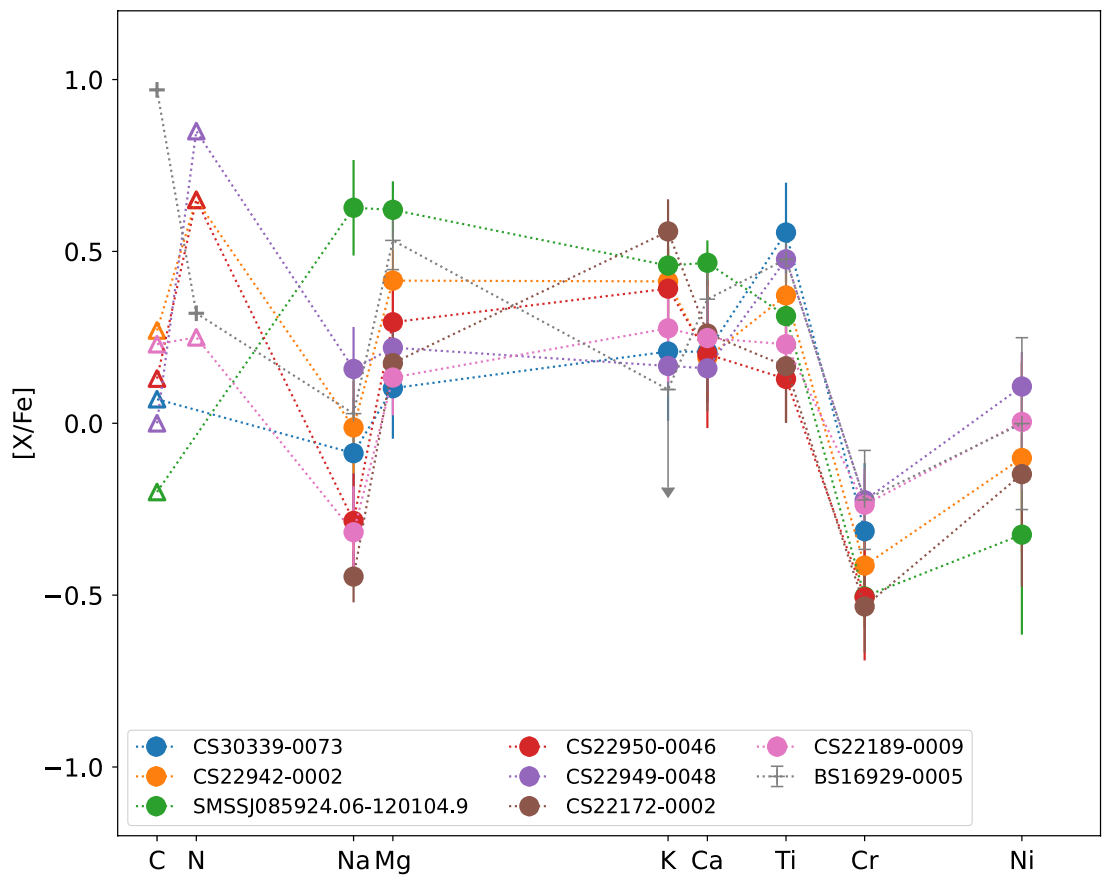


Figure 7. The abundance pattern of stars with estimated K abundances. The gray crosses indicate the abundance pattern of BS 16929–0005, whose upper limits were found to be lower than the typical [K/Fe] values. The abundances of C and N are taken from the literature (see the text for details).

the [K/Ca] case, the model with $M=13M_{\odot}$ and $V_{\rm rot}=300\,{\rm km\,s^{-1}}$ best reproduces not only the [K/Fe] ratios but also the ratios of [Sc/Fe] and [Mn/Fe]. The 15 M_{\odot} model with $V_{\rm rot}=300\,{\rm km\,s^{-1}}$ tends to overproduce all of these abundance ratios relative to the fixed amount of Fe (produced as $^{56}{\rm Ni}$) assumed in this model set. Across all rotational velocities, the models generally predict either no correlation or a weak positive correlation between [K/Fe] and [Mn/Fe], which is inconsistent with the tentative anticorrelation as suggested in the lower-left panel of this figure.

L. Roberti et al. (2024) attributed the enhanced synthesis of oxygen-burning products, including K, in metal-free $M = 15_{\odot}$ rotating star yield models to the mixing between the convective O shell and the products of C-shell burning. Their calculations include stellar evolution and explosion yields for massive stars (15 and 25 M_{\odot}) across a wide range of initial rotational velocities (0-800 km s⁻¹) and metallicities ([Fe/ H] = $-\infty$, -5, -4). The enhancement of oxygen-burning products is found to occur regardless of the progenitor's metallicity. Under the proposed scenario involving the C-O shell merger, the oxygen-burning products are less likely to undergo further processing via explosive nucleosynthesis during the supernova and are instead ejected (L. Roberti et al. 2024). This scenario may also explain the observed variation in the Na/Mg ratios among the stars analyzed in this study, which could reflect differing degrees of these mixing processes during the final phase of stellar evolution (L. Roberti et al. 2024). Interactions between oxygen and carbon shells in massive stars have also been suggested to explain the observed

abundance patterns of other odd-Z elements, such as phosphorus (P) and chlorine (Cl) (C. Ritter et al. 2018).

In summary, rotating massive stars could account for the observed abundances of K and other odd-Z elements in the sample stars if the ejecta from rotating massive stars with rotational velocities as high as 300 km s⁻¹ significantly contributed to the enrichment of the interstellar medium. Further examination of this scenario through homogeneous analysis of CNO as well as neutron-capture elements would be necessary to confirm this scenario.

5.2.2. The Innermost Region of CCSNe

Another possible site of K production has been suggested as explosive oxygen burning in the innermost regions of core-collapse supernovae. The nucleosynthesis yields of these mechanisms are difficult to predict because of the uncertainty in the mechanism of supernova explosion.

The square symbols in Figure 9 show the predicted CCSN yields of zero-metallicity nonrotating massive stars from A. Heger & S. E. Woosley (2010), which includes ν -process with assumed temperature and fluxes of neutrinos. We plotted the yields with an assumed mass cut at the base of the oxygen shell ("S4" model) with no mixing of ejecta. The models with extremely low yield of Ca $<10^{-5}M_{\odot}$ are excluded from this plot. The different colors correspond to the differences in the explosion energy, $E_{51}=0.3, 1.2$, and 10.0. The size of the symbols represents progenitor stellar masses M=10, 20, 30, 40, 80, and $100M_{\odot}$, where larger symbols correspond to higher stellar masses.

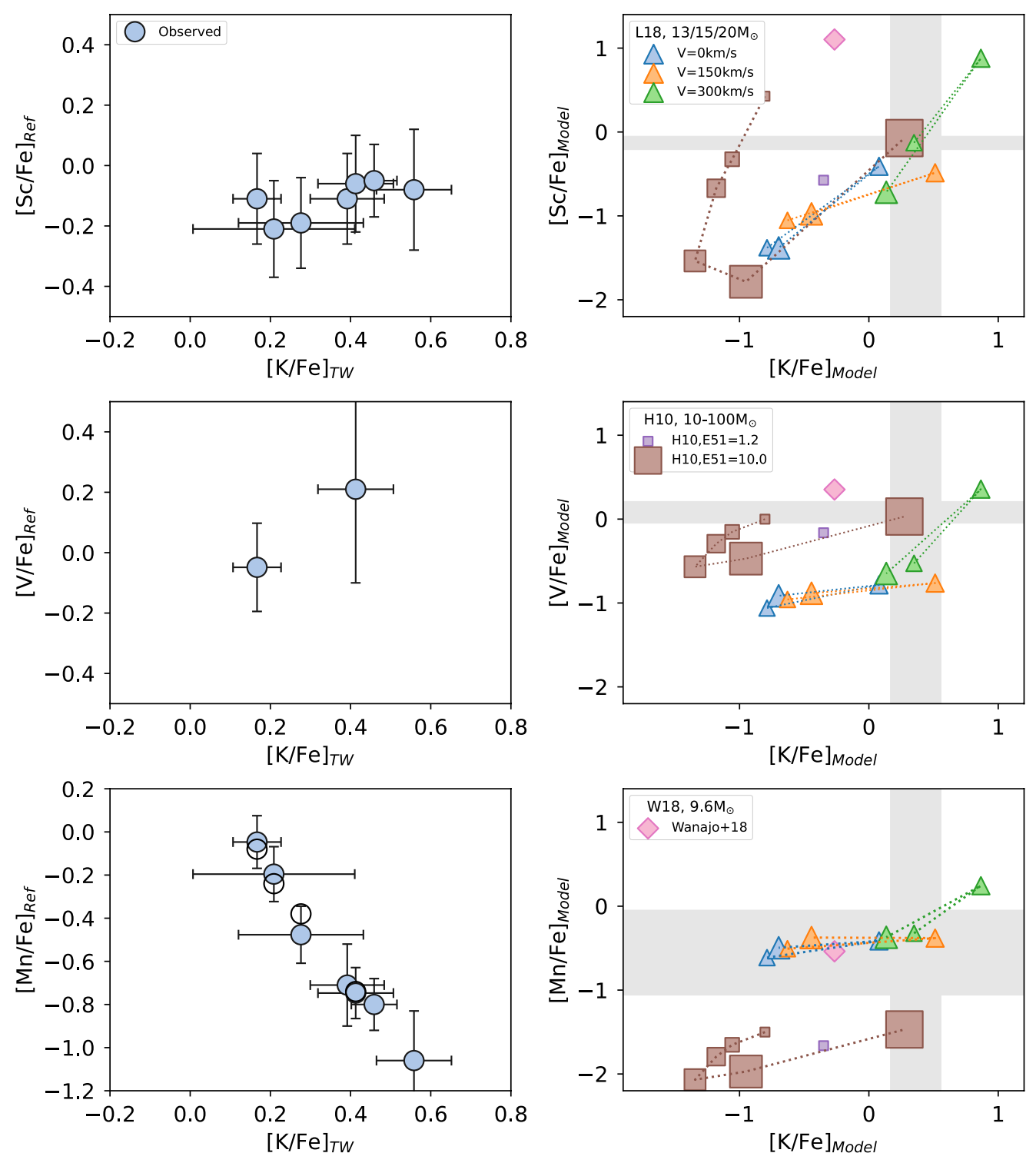


Figure 8. Left: the [Sc/Fe], [V/Fe], and [Mn/Fe] ratios adopted from the literature plotted against [K/Fe]_{NLTE} derived in this study. In the bottom-left panel for the [Mn/Fe] ratios plotted against [K/Fe]_{NLTE}, we also show [Mn/Fe] ratios obtained using Mn II lines only by I. U. Roederer et al. (2014) for four of the sample stars in open circles. Right: the predicted theoretical yields of odd-Z elements. Triangles are the rotating massive star yield model by M. Limongi & A. Chieffi (2018). The models with initial rotational velocities of 0, 150, and 300 km s⁻¹ are shown by blue, orange, and green triangles, respectively. For each rotational velocity, the models with three different progenitor masses, M = 13, 15, and $20M_{\odot}$, are shown, where the larger symbol corresponds to a more massive model. Squares indicate the nonrotating supernova yield models with explosion energies of $E_{51} = 1.2$ and 10 from A. Heger & S. E. Woosley (2010). The symbol size represents the progenitor mass from 10 to $100M_{\odot}$. The diamond shows the yields from the two-dimensional core-collapse supernova simulation of a $9.6M_{\odot}$ star by S. Wanajo et al. (2018). The observed range of each of the abundance ratios is shown by a vertical or horizontal gray band.

The model with a progenitor mass of $10M_{\odot}$ and explosion energy $E_{51}=0.3$ predicts a K yield on the order of $\sim 10^{-6}M_{\odot}$, which overlaps within 1σ of observed abundances. The models

with the same stellar mass and higher explosion energies predict the K yield of 10^{-6} – $10^{-5}M_{\odot}$, while the larger Ca yield in these models lead to [K/Ca] ratios much lower than the

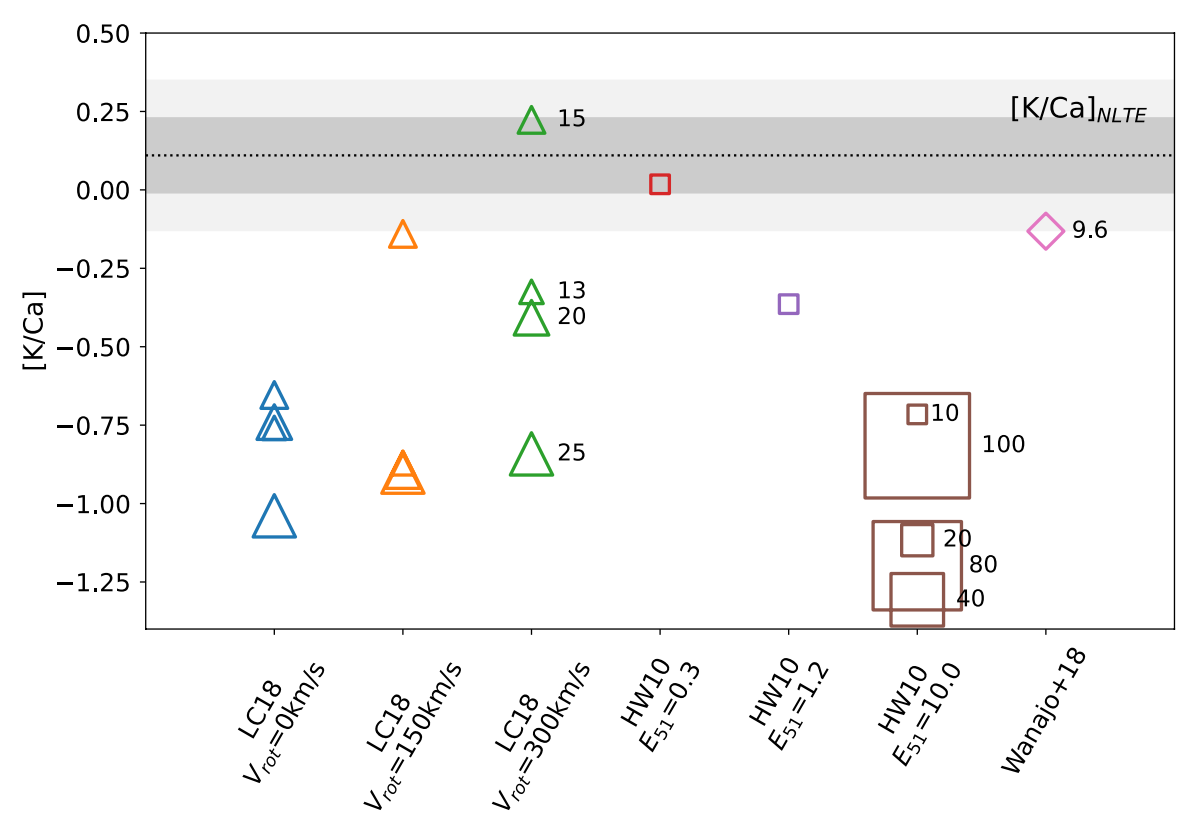


Figure 9. [K/Ca] abundance ratios predicted by core-collapse supernova yields in literature. Triangles correspond to the CCSN yields of rotating massive stars from M. Limongi & A. Chieffi (2018) with rotational velocity $V_{\rm rot}=0$ (blue), 150 (orange), and 300 (green) km s⁻¹, respectively. The size of the symbols represents progenitor masses of 13, 15, 20, and 25 M_{\odot} and is indicated on the right-hand side of each symbol. Squares correspond to the CCSN yields of nonrotating zero-metallicity stars from A. Heger & S. E. Woosley (2010) with various supernova explosion energies. The size of the symbols represents progenitor masses of $10-100M_{\odot}$ and is indicated on the right-hand side of each symbol. The diamond corresponds to the CCSN yields of a zero-metallicity $M=9.6M_{\odot}$ star based on a 2D simulation by S. Wanajo et al. (2018). The mean of observed abundances (of seven stars) and their 1σ (dark gray) and 2σ (light gray) are shown by gray horizontal bands

observed values.

Figure 8 shows the correlation between the predicted [K/Fe] ratios and the abundance ratios of other odd-Z elements from the literature. The model with a progenitor mass of $10M_{\odot}$ and explosion energy $E_{51}=0.3$ predicts extremely small Fe yields, and therefore incompatible with any of the abundance ratios shown in this figure. Instead, the model with high explosion energy $E_{51}=10.0$ and a progenitor mass of $100M_{\odot}$ predicts [Sc/Fe] and [V/Fe] as well as the [K/Fe] ratios that are compatible with the data. All models underestimate the [Mn/Fe] ratios.

It has long been recognized that the discrepancy between observed abundances and theoretical yield models based on one-dimensional core-collapse supernova simulations is due to the uncertainty in the elemental yields in the innermost region of the exploding star, which depends on the physical mechanism relevant to interactions between neutrinos and nucleons (C. Fröhlich et al. 2006; S. Wanajo et al. 2018). T. Yoshida et al. (2008) also suggest that the ν -process in corecollapse supernovae of Population III stars produce odd-Z elements such as K, Sc, V, and Mn (T. Yoshida et al. 2008; C. Kobayashi et al. 2011). With the ν -process, the predicted values of [Mn/Fe] are enhanced to reconcile with the observed abundance ratios of EMP stars.

To accurately predict the yields of K in the innermost regions of core-collapse supernovae, multidimensional hydrodynamical simulations are necessary. S. Wanajo et al. (2018) carried out nucleosynthesis calculations in the innermost,

neutrino-heated ejecta from several two-dimensional, self-consistently exploding models of core-collapse supernovae, from which we adopt the model yields of the zero-metallicity star with an initial mass of $9.6M_{\odot}$ ("z9.6" model). Potassium synthesis appears to be strongly dependent on Y_e , and thus can be a tracer to test such multidimensional models. In their simulation, K is synthesized under proton-rich ($Y_e > 0.5$) conditions in the innermost ejecta, while Ca is predominantly produced at $Y_e \sim 0.5$. Under such conditions, nucleosynthesis does not depend on the composition prior to the explosion, as the interaction between neutrinos and nucleons redetermines the electron fraction Y_e . This scenario of nucleosynthesis in neutrino-processed ejecta is also supported by recent X-ray measurements of supernova remnants (T. Sato et al. 2023).

The predicted abundance ratio [K/Ca] is shown in Figure 9 as a diamond symbol. The K and Ca yields from this simulation are $M=3.37\times 10^{-6}M_{\odot}$ and $M=9.58\times 10^{-5}M_{\odot}$, both of which are compatible with the observed ratios [K/H] and [Ca/H] if the ejecta are mixed with hydrogen of $10^3-10^4M_{\odot}$, although the [K/Ca] ratio is smaller than the observational values. This implies that the innermost ejecta of typical core-collapse supernovae are dominated by more proton-rich ejecta than in the model adopted here. The result of the small K abundance scatter, despite a large scatter in the lighter elements, is also in line with this prediction from the K production in neutrino-processed ejecta, where the yields are mainly determined by the physical conditions in the innermost ejecta of core-collapse supernovae with little dependence on

progenitor masses or metallicities. The predicted abundance ratios for other odd-Z elements are shown in the right panels of Figure 8. The model underproduces [K/Fe] ratios, while the [Mn/Fe] ratio is within the observed range.

Overall, none of the yield models of K synthesis in corecollapse supernovae examined in this section simultaneously reproduce the observed abundance ratios of K, Sc, V, and Mn. Furthermore, the ν -process suggested to be the site of some of the odd-Z elements generally predicts a positive correlation between K and Mn abundance ratios, which is incompatible with the hint of anticorrelation observed among stars with a detected K I line. Multidimensional simulations for a wide range of progenitor masses and explosion energies, taking into account the ν -process in a self-consistent manner, would be essential to obtain a consensus on the origin of K at the lowest metallicity regime.

6. Conclusion

We revisited the abundances of potassium (K) in extremely metal-poor stars based on a new homogeneous analysis of K abundances derived from high-resolution spectra obtained with Subaru/HDS. NLTE corrections from H. Reggiani et al. (2019) were applied to derive the NLTE abundances based on the K I 766/769 nm resonance lines. This study demonstrates that the correlation between K abundances and other elemental abundance ratios in EMP stars provides important constraints on the late stages of massive stellar evolution and the unknown mechanisms of supernova explosions, both of which are inaccessible to direct observation and are challenging to theoretically simulate from first principles.

Our main findings can be summarized below.

- 1. Among the seven stars with [Fe/H] < -3 with measured K abundances, the scatters in the [K/Fe] and [K/Ca] ratios is as small as the typical measurement uncertainty. After the NLTE correction, the mean abundance is in good agreement with the previous analysis of the NLTE K abundance by Y. Takeda et al. (2009) and H. Reggiani et al. (2019).
- 2. The observed upper limits of the K abundance ratios are $[K/Fe]_{NLTE} < 0.8$ dex and $[K/Ca]_{NLTE} < 0.7$, respectively, for most of the sample stars.
- 3. Despite the uniformity of the [K/Fe] and [K/Ca] ratios, the [Na/Mg] ratios show a scatter of 0.7 dex, which could be caused by variations in progenitor mass, metallicity of core-collapse supernovae, or the various degrees of mixing of different layers at the end of massive star evolution. This suggests that the nucleosynthesis site of K is likely independent of those other properties.
- 4. An apparent anticorrelation between the [K/Fe] and [Mn/Fe] abundance ratios has been identified. If this trend is confirmed with a larger statistical sample and reduced systematic uncertainties, it would provide a valuable diagnostic of the physical conditions governing the nucleosynthesis of these elements in the early Universe.

The uniform abundance ratios of [K/Ca] among the EMP stars might suggest a universal origin of K at the lowest [Fe/H] regime. The comparison of the observed [K/Ca] ratios with nucleosynthesis yield models of massive stars suggests that,

depending on the progenitor masses, rotational velocities, or explosion energies, some of the hydrostatic burning or corecollapse supernovae of (non)rotating massive stars could be the site of K synthesis together with Ca. However, none of the yield models simultaneously reproduces all of the observed abundances of odd-Z elements.

To obtain a robust conclusion on the nucleosynthesis sites of K, together with other odd-Z elements, a tighter constraint on the K abundance upper limits and a statistical sample of EMP stars with detailed elemental abundances are both important. Updated theoretical insights from multidimensional effects in stellar evolution and core-collapse supernova explosions are also crucial to ultimately constraining the K synthesis sites, which may be related to yet unknown physical mechanisms of dying massive stars.

Acknowledgments

We are grateful to the anonymous referee for helpful suggestions, which significantly improved the quality of this paper. We thank Y. Takeda for his advice on proposal preparation and abundance analysis. We thank S. Katsuda, L. Roberti, and A. Karakas for their valuable discussions and constructive suggestions, which have greatly improved this work. M.N.I. would like to thank S. Hong for her valuable contributions to the data analysis and discussions. This work was supported by JSPS KAKENHI grant Nos. JP25K01046, JP23KF0290, JP21H04499, and JP20H05855. This work is based on observations made with the Subaru Telescope, operated by the National Astronomical Observatory of Japan. We are grateful to the observatory staff for their support during the observations. This work has made use of the VALD database, operated at Uppsala University, the Institute of Astronomy RAS in Moscow, and the University of Vienna.

Facility: Subaru.

Software: astropy (P. Greenfield et al. 2013), IRAF (D. Tody 1993), PyRAF (Science Software Branch at STScI 2012), iSpec (S. Blanco-Cuaresma et al. 2014; S. Blanco-Cuaresma 2019), Turbospectrum (B. Plez 2012).

ORCID iDs

Miho N. Ishigaki https://orcid.org/0000-0003-4656-0241 Nozomu Tominaga https://orcid.org/0000-0001-8537-3153 Wako Aoki https://orcid.org/0000-0002-8975-6829 Shinya Wanajo https://orcid.org/0000-0002-4759-7794 Tomoya Takiwaki https://orcid.org/0000-0003-0304-9283 Ko Nakamura https://orcid.org/0000-0002-8734-2147 Ken'ichi Nomoto https://orcid.org/0000-0001-9553-0685 Chiaki Kobayashi https://orcid.org/0000-0002-4343-0487

References

Andrievsky, S. M., Spite, M., Korotin, S. A., et al. 2010, A&A, 509, A88
Aoki, W., Beers, T. C., Christlieb, N., et al. 2007, ApJ, 655, 492
Aoki, W., Beers, T. C., Lee, Y. S., et al. 2013, AJ, 145, 13
Audouze, J., & Silk, J. 1995, ApJL, 451, L49
Bailer-Jones, C. A. L., Rybizki, J., Fouesneau, M., Demleitner, M., & Andrae, R. 2021, AJ, 161, 147
Bergemann, M., Gallagher, A. J., Eitner, P., et al. 2019, A&A, 631, A80
Blanco-Cuaresma, S. 2019, MNRAS, 486, 2075
Blanco-Cuaresma, S., Soubiran, C., Heiter, U., & Jofré, P. 2014, A&A, 569, A111
Bollig, R., Yadav, N., Kresse, D., et al. 2021, ApJ, 915, 28
Casagrande, L., Lin, J., Rains, A. D., et al. 2021, MNRAS, 507, 2684
Cayrel, R., Depagne, E., Spite, M., et al. 2004, A&A, 416, 1117

```
Cohen, J. G., Christlieb, N., Thompson, I., et al. 2013, ApJ, 778, 56
Cohen, J. G., Huang, W., & Kirby, E. N. 2011, ApJ, 740, 60
Demarque, P., Woo, J.-H., Kim, Y.-C., & Yi, S. K. 2004, ApJS, 155, 667
Fernández-Alvar, E., Allende Prieto, C., Beers, T. C., et al. 2016, A&A,
  593. A28
Fröhlich, C., Hauser, P., Liebendörfer, M., et al. 2006, ApJ, 637, 415
Green, G. 2018, JOSS, 3, 695
Green, G. M., Schlafly, E., Zucker, C., Speagle, J. S., & Finkbeiner, D. 2019,
   ApJ, 887, 93
Greenfield, P., Robitaille, T., Tollerud, E. et al., 2013, Astropy: Community
   Python library for astronomy, 545 Astrophysics Source Code Library, ascl:
Gustafsson, B., Edvardsson, B., Eriksson, K., et al. 2008, A&A, 486, 951
Heger, A., & Woosley, S. E. 2010, ApJ, 724, 341
Heiter, U., Lind, K., Bergemann, M., et al. 2021, A&A, 645, A106
Holtzman, J. A., Hasselquist, S., Shetrone, M., et al. 2018, AJ, 156, 125
Ishigaki, M. N., Aoki, W., & Chiba, M. 2013, ApJ, 771, 67
Ishigaki, M. N., Chiba, M., & Aoki, W. 2012, ApJ, 753, 64
Ishigaki, M. N., Tominaga, N., Kobayashi, C., & Nomoto, K. 2018, ApJ,
   857, 46
Iwamoto, N., Umeda, H., Nomoto, K., et al. 2006, in AIP Conf. Ser. 847,
   Origin of Matter and Evolution of Galaxies, ed. S. Kubono et al. (Melville,
   NY: AIP), 409
Jacobson, H. R., Keller, S., Frebel, A., et al. 2015, ApJ, 807, 171
Kobayashi, C., Izutani, N., Karakas, A. I., et al. 2011, ApJ, 739, L57
Kobayashi, C., Karakas, A. I., & Lugaro, M. 2020, ApJ, 900, 179
Kotake, K., Sumiyoshi, K., Yamada, S., et al. 2012, PTEP, 2012, 01A301
Koutsouridou, I., Skúladóttir, Á., & Salvadori, S. 2025, A&A, 699, A32
Kupka, F., Piskunov, N., Ryabchikova, T. A., Stempels, H. C., &
   Weiss, W. W. 1999, A&AS, 138, 119
Lai, D. K., Bolte, M., Johnson, J. A., et al. 2008, ApJ, 681, 1524
Li, H., Aoki, W., Matsuno, T., et al. 2022, ApJ, 931, 147
Limongi, M., & Chieffi, A. 2018, ApJS, 237, 13
Lind, K., Nordlander, T., Wehrhahn, A., et al. 2022, A&A, 665, A33
Martin, N. F., Starkenburg, E., Yuan, Z., et al. 2024, A&A, 692, A115
Mucciarelli, A., Bellazzini, M., Ibata, R., et al. 2012, MNRAS, 426
  2889
Nakamura, K., Takiwaki, T., Matsumoto, J., & Kotake, K. 2025, MNRAS,
   536, 280
Nguyen, C. T., Costa, G., Girardi, L., et al. 2022, A&A, 665, A126
```

Nissen, P. E., Hoeg, E., & Schuster, W. J. 1997, in ESA SP-402, Proc. of the

Noguchi, K., Aoki, W., Kawanomoto, S., et al. 2002, PASJ, 54, 855

Nomoto, K., Kobayashi, C., & Tominaga, N. 2013, ARA&A, 51, 457

ESA), 225

ESA Symp. The Hipparcos - Venice '97, ed. R. M. Bonnet et al. (Paris:

```
Jeffery, C. S. 1995, A&As, 112, 525
Placco, V. M., Frebel, A., Beers, T. C., & Stancliffe, R. J. 2014, ApJ, 797, 21
Placco, V. M., Frebel, A., Lee, Y. S., et al. 2015, ApJ, 809, 136
Plez, B. 2012, Turbospectrum: Code for Spectral Synthesis, Astrophysics
  Source Code Library, ascl:1205.004
Prantzos, N., Abia, C., Limongi, M., Chieffi, A., & Cristallo, S. 2018,
          S, 476, 3432
Reggiani, H., Amarsi, A. M., Lind, K., et al. 2019, A&A, 627, A177
Ritter, C., Andrassy, R., Côté, B., et al. 2018, MNRAS, 474, L1
Roberti, L., Limongi, M., & Chieffi, A. 2024, ApJS, 270, 28
Roederer, I. U., Preston, G. W., Thompson, I. B., et al. 2014, AJ, 147, 136
Ryabchikova, T., Piskunov, N., Kurucz, R. L., et al. 2015, PhyS, 90, 054005
Sato, T., Matsunaga, K., Uchida, H., et al. 2025, ApJ, 990, 103
Sato, T., Yoshida, T., Umeda, H., et al. 2023, ApJ, 954, 112
Schlafly, E. F., & Finkbeiner, D. P. 2011, ApJ, 737, 103
Science Software Branch at STScI, 2012, PyRAF: Python638 alternative for
  IRAF, Astrophysics Source Code Library, ascl:1207.011
Sieverding, A., Kresse, D., & Janka, H.-T. 2023, ApJL, 957, L25
Sumiyoshi, K., Yamada, S., Suzuki, H., et al. 2005, ApJ, 629, 922
Takahashi, K., Umeda, H., & Yoshida, T. 2014, ApJ, 794, 40
Takeda, Y., Kaneko, H., Matsumoto, N., et al. 2009, PASJ, 61, 563
Takeda, Y., Zhao, G., Chen, Y.-Q., Qiu, H.-M., & Takada-Hidai, M. 2002,
Takiwaki, T., Kotake, K., & Suwa, Y. 2014, ApJ, 786, 83
Timmes, F. X., Woosley, S. E., & Weaver, T. A. 1995, ApJS, 98, 617
Tody, D. 1993, in ASP Conf. Ser. 52, Astronomical Data Analysis Software
  and Systems II, ed. R. J. Hanisch, R. J. V. Brissenden, & J. Barnes (San
  Francisco, CA: ASP), 173
Tominaga, N., Iwamoto, N., & Nomoto, K. 2014, ApJ, 785, 98
Tominaga, N., Umeda, H., & Nomoto, K. 2007, ApJ, 660, 516
Umeda, H., & Nomoto, K. 2005, ApJ, 619, 427
Vartanyan, D., Tsang, B. T. H., Kasen, D., et al. 2025, ApJ, 982, 9
Wanajo, S., Janka, H.-T., & Müller, B. 2011, ApJL, 726, L15
Wanajo, S., Müller, B., Janka, H.-T., & Heger, A. 2018, ApJ, 852, 40
Wang, T., & Burrows, A. 2024, ApJ, 974, 39
Woosley, S. E., Heger, A., & Weaver, T. A. 2002, RvMP, 74
  1015
Woosley, S. E., & Weaver, T. A. 1995, ApJS, 101, 181
Yi, S. K., Kim, Y.-C., Demarque, P., et al. 2008, in IAU Symp. 252, The Art
  of Modeling Stars in the 21st Century, ed. L. Deng & K. L. Chan
  (Cambridge: Cambridge Univ. Press), 413
Yong, D., Norris, J. E., & Bessell, M. S. 2013, ApJ, 762, 26
Yoshida, T., Umeda, H., & Nomoto, K. 2008, ApJ, 672, 1043
Zhao, G., Mashonkina, L., Yan, H. L., et al. 2016, ApJ, 833, 225
```

Piskunov, N. E., Kupka, F., Ryabchikova, T. A., Weiss, W. W., &